Understanding Chemical Shielding Tensors Using Group Theory, MO Analysis, and Modern Density-Functional Theory

CORY M. WIDDIFIELD, ROBERT W. SCHURKO

Department of Chemistry and Biochemistry, University of Windsor, Windsor, ON N9B 3P4, Canada

ABSTRACT: In this article, the relationships between molecular symmetry, molecular electronic structure, and chemical shielding (CS) tensors are discussed. First, a brief background on the CS interaction and CS tensors is given. Then, the visualization of the three-dimensional nature of CS is described. A simple method for examining the relationship between molecular orbitals (MOs) and CS tensors, using point groups and direct products of irreducible representations of MOs and rotational operators, is outlined. A number of specific examples are discussed, involving CS tensors of different nuclei in molecules of different symmetries, including ethene (D_{2h}), hydrogen fluoride ($C_{\infty v}$), trifluorophosphine (C_{3v}), and water (C_{2v}). Finally, we review the application of this method to CS tensors in several interesting cases previously discussed in the literature, including acetylene ($D_{\infty h}$), the PtX_4^{2-} series of compounds (D_{4h}) and the decamethylaluminocenium cation (D_{5d}). © 2009 Wiley Periodicals, Inc. Concepts Magn Reson Part A 34A: 91–123, 2009.

KEY WORDS: chemical shielding; chemical shift; chemical shielding tensor; symmetry; first principles calculations; DFT calculations; group theory; direct product

INTRODUCTION

The chemical shift, δ, is considered by many chemists to be the most important NMR parameter for the structural characterization of matter at the molecular level (*1, 2*). Ramsey and Pople (*3–7*) provided a theoretical foundation for the calculation of chemical shielding (CS) in atomic and molecular systems shortly after the initial observations of frequency-shifted resonances (i.e., chemical shifts) (*8, 9*); however, the accurate calculation of unknown chemical
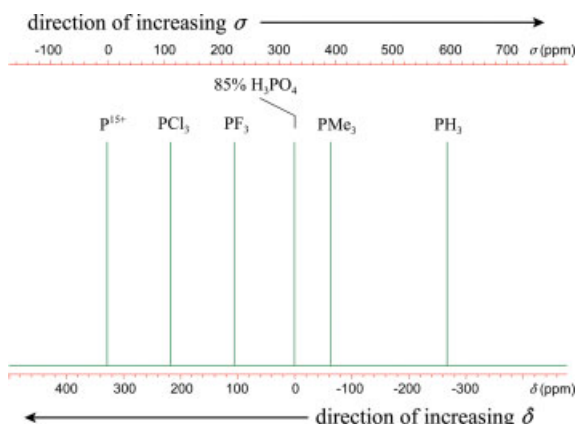
Figure 1 Comparison of chemical shielding, σ, and chemical shift, δ, scales using a portion of the phosphorus absolute shielding scale developed by Jameson et al. (*10*). The scales are calibrated such that $\sigma(P^{15+}) = 0.0$ ppm and $\delta(85\% \; H_3PO_4(aq)) = 0.0$ ppm. [Color figure can be viewed in the online issue, which is available at www.interscience.wiley.com.]

shift values has proven to be a substantial challenge. A theoretically calculated CS value, σ, describes the degree of magnetic shielding at a nuclear centre in a molecule/atom with respect to the bare nucleus, and is related to an experimentally observable chemical shift, δ:

$$\delta \equiv \frac{\sigma_{\text{ref}} - \sigma}{1 - \sigma_{\text{ref}}} \qquad (1)$$

where σ_{ref} is the shielding value associated with a nucleus for an arbitrarily chosen reference sample. For a chemical shift value to be determined theoretically (i.e., to relate chemical shift and CS), shielding values for both the unknown and a reference compound are required. Absolute shielding scales, which organize information much like chemical shift scales (Fig. 1), have been established for several nuclides using experimental data or one of a number of hybrid experimental–theoretical methods (*11–17*). Purely computational approaches have not developed to the point where they may be used to quantitatively produce an absolute shielding scale; however, calculated shielding values are constantly improving (*18–22*), as solutions pertaining to gauge variance (*23–28*), relativistic effects (*29–33*), and electron correlation (*34, 35*) problems have been formulated and improvements in computational capacity allow for the use of increasingly complex basis sets.

Hence, although the physical origins of CS have been fully described and significant progress has been made toward the theoretical prediction of CS,

the accurate calculation of CS parameters remains daunting (*22, 36*). There is great interest in the accurate computation of shielding parameters, as anisotropic chemical shift parameters have been experimentally measured in a variety of systems, and are of great importance in the accurate interpretation of molecular structure. It is also of value to understand both the origins of observed chemical shifts and how chemical shifts are influenced by structure, bonding, and molecular symmetry. With such knowledge, chemists and biochemists can make sound structural predictions from experimental solution and solid-state NMR (ssNMR) data.

Herein, we present a short background on CS, and a detailed discussion outlining a basic framework for understanding and visualizing the relationships between electronic structure, molecular symmetry, and chemical shielding anisotropy (CSA). It is noted that aspects of this discussion can be found elsewhere in the literature, including: i) how the current density induced by the applied magnetic field is related to observable chemical shifts (*6, 37*); ii) that atomic orbitals (AOs) and molecular orbitals (MOs) can be used to rationalize the origin of the induced current (*38–44*); and iii) that symmetry arguments can be used to determine allowed and forbidden contributions to CS from magnetically induced mixing of MOs (*45–48*).

We demonstrate that the rotational operators, $(\hat{R}_n)$, common to group theory, belong to the same irreducible representations (IRs) as the quantum-mechanical angular momentum operators, $(\hat{L}_n)$, which are used in Ramsey's formalism for CS. Using simple symmetry arguments, these rotational operators can be used to qualitatively determine which MOs make contributions to the CS tensor. The procedure is shown to be analogous to the evaluation of three-centre integrands of transition moments in optical and vibrational spectroscopy, which involves the IRs of two MOs and the electric dipole moment operator, $\hat{\mu}$; however, we stress that the physical origins of these integrals are completely distinct.

In addition, CS tensors are calculated for molecules of differing symmetry using software that employs gauge-including AO (GIAO) (*23*) basis sets and modern density-functional theory (DFT) methods (*49–51*). The principal components of the CS tensors are decomposed, in a similar fashion to Ramsey (*3*), into diamagnetic and paramagnetic contributions. Consideration of the molecular and nuclear site symmetries, and the symmetry of the rotational operators, provides a means of visualizing and predicting the contributions to the components of the CS tensor, and ultimately to the observed chemical shifts.

BACKGROUND

The CS Interaction

When a molecule is placed in an external magnetic field, $\mathbf{B}_0$, local magnetic fields are induced in the molecule, which serve to reduce (shield) or increase (deshield) the net magnetic fields at the nuclear sites, resulting in frequency shifts in the NMR spectrum. The magnitudes of these induced local fields depend on the identity of the nucleus being observed (i.e., gyromagnetic ratio, γ), the electronic structure of the molecule, as well as the orientation of the molecule with respect to $\mathbf{B}_0$. Again, we note here for clarity that CS (denoted with σ) describes the magnetic shielding at a nuclear site with respect to the bare nucleus ($\sigma_{\text{bare}} = 0$ ppm), with increasing magnetic shielding described by increasingly positive values of σ. On the other hand, *chemical shifts* (denoted with δ) are measured in NMR experiments with respect to a standard reference; however, increasingly positive values of δ indicate magnetic deshielding. The CS and chemical shifts are related by [1]. The CS interaction is anisotropic (i.e., CSA), and the range of chemical shifts arising from this orientation dependence is observed in NMR experiments as chemical shift anisotropy (δ_{CSA}). Microcrystalline powders typically have a random distribution of crystallite orientations with respect to $\mathbf{B}_0$. Hence, in the ssNMR spectra of such powders, each magnetically distinct nucleus gives rise to a unique δ_{CSA} powder pattern. These powder patterns are rich in information pertaining to molecular structure; however, because they are often very broad, both the spectral resolution and achievable signal-to-noise (S/N) ratio are reduced. The S/N ratio may be increased, and resolution may be recovered, using a number of techniques, such as sample rotation about single (e.g., magic-angle spinning) (*52*, *53*) or multiple-axes (*54–57*), or other correlation experiments (*58–60*). It should be noted that numerous pulse sequences have been developed for retaining δ_{CSA} information (*61–75*); however, this discussion is beyond the scope of this article.

The CS Hamiltonian and Tensor Conventions

The Hamiltonian (in units of rad s^{-1}) used to describe the CS interaction is as follows:

$$\hat{\mathcal{H}}_{\text{CS}} = \gamma \mathbf{B}_0 \cdot \ddot{\sigma} \cdot \hat{I}, \tag{2}$$

where γ is the gyromagnetic ratio, $\hat{I}$ is the nuclear spin operator, and $\ddot{\sigma}$ is the CS tensor (vectors are denoted in boldface, and tensors are denoted using an umlaut). The CS tensor describes the magnitude and orientation dependence of the CS interaction and can be represented in 3D Cartesian space using a 3 × 3 matrix (*76*):

$$\ddot{\sigma} = \begin{bmatrix} \sigma_{xx} & \sigma_{xy} & \sigma_{xz} \\ \sigma_{yx} & \sigma_{yy} & \sigma_{yz} \\ \sigma_{zx} & \sigma_{zy} & \sigma_{zz} \end{bmatrix}. \tag{3}$$

Each element, σ_{ij} ($i, j = x, y, z$), represents the i-component of shielding when $\mathbf{B}_0$ is applied along the j-axis and can be related to an observable chemical shift component according to the relationship shown below:

$$\delta_{ij} = \frac{\sigma_{\text{iso,ref}} - \sigma_{ij}}{1 - \sigma_{\text{iso,ref}}}, \tag{4}$$

where δ_{ij} is the ij-component of the chemical shift tensor and $\sigma_{\text{iso,ref}}$ is the isotropic shielding value for an arbitrary reference compound. The CS tensor is asymmetric; however, the observable first-order (i.e., secular) response is symmetric (*77*) (hence $\delta_{ij} = \delta_{ji}$). The antisymmetric portion of the tensor, which is contained in the second-order shielding response that is perpendicular to the applied field (*77*, *78*), has never been definitively observed in ssNMR powder patterns (*79*) and is omitted from subsequent discussion. The symmetric portion of the CS tensor can be diagonalized into its own principal axis system

$$\ddot{\sigma}_{\text{PAS}} = \begin{bmatrix} \sigma_{11} & 0 & 0 \\ 0 & \sigma_{22} & 0 \\ 0 & 0 & \sigma_{33} \end{bmatrix} \tag{5}$$

with the set of diagonal elements (i.e., the eigenvalues) being referred to as the principal components. By convention, the principal components are assigned such that $\sigma_{11} \leq \sigma_{22} \leq \sigma_{33}$, with σ_{11} being the least shielded tensor component. Each principal component corresponds to a unique shielding direction (i.e., an eigenvector or principal axis). The set of three eigenvectors forms an orthogonal, three-dimensional basis. In this manuscript, $\boldsymbol{\sigma}_{11}$ (in boldface type) will represent the direction of least shielding, $\boldsymbol{\sigma}_{22}$ will represent the direction of intermediate shielding, and $\boldsymbol{\sigma}_{33}$ will represent the direction of greatest shielding. The isotropic CS value, σ_{iso}, is defined as:

$$\sigma_{\text{iso}} = \frac{1}{3} \text{ Tr } \{\ddot{\sigma}\} \equiv \frac{1}{3}(\sigma_{11} + \sigma_{22} + \sigma_{33}), \tag{6}$$

is independent of the chosen reference frame (i.e., the trace of [3] equals that of [5]), and is related to the isotropic chemical shift, δ_{iso}, by equation [1]. The

isotropic chemical shift is the parameter observed in most NMR experiments on samples in nonviscous solvents, due to averaging of δ_{CSA} by rapid and random molecular tumbling.

Three conventions are commonly used when reporting CS/shift tensors (*80*). The formalism discussed earlier (i.e., $\sigma_{11} \leq \sigma_{22} \leq \sigma_{33}$) is known as the frequency-ordered principal shift values convention (*81*). The Maryland Group defined two additional parameters (*80*, *82*): span, Ω, and skew, κ, which describe the magnitude of the CSA and degree of axial symmetry of the CS tensor, respectively,

$$\Omega \equiv \sigma_{33} - \sigma_{11} \approx \delta_{11} - \delta_{33};$$

$$\kappa \equiv \frac{3(\sigma_{iso} - \sigma_{22})}{\Omega} \approx \frac{3(\delta_{22} - \delta_{iso})}{\Omega}, \quad (7)$$

where Ω is a positive value in units of ppm and κ is a value ranging from +1 to –1. This convention will be used herein, because of its unambiguous labelling of the principal components. It is important to note that though the shielding relationships in [7] are exact, the shift relationships are not. For very large (>1,000 ppm) shift values, [4] should be used explicitly for each component. Finally, it should be mentioned that the "Haeberlen–Mehring–Spiess" convention (*76*, *83*, *84*) (commonly referred to as the Haeberlen convention) defines the shielding anisotropy, $\Delta\sigma$, and asymmetry, η, parameters, using principal components that are defined differently in comparison with the previous conventions (Fig. 2):

$$|\Delta\sigma| \equiv \sigma_{ZZ} - \frac{\sigma_{XX} + \sigma_{YY}}{2} \; ; \quad \eta = \frac{\sigma_{YY} - \sigma_{XX}}{\sigma_{ZZ} - \sigma_{iso}}, \quad (8)$$

where $|\sigma_{ZZ-iso}| \geq |\sigma_{XX-iso}| \geq |\sigma_{YY-iso}|$. Although this notation uses *X*, *Y*, and *Z* labels, reference is not being made to the molecular frame, but to the arbitrary definitions for the components listed earlier. The Haeberlen convention is not referred to later in this work: for further details, the reader is referred to the literature (*80*, *83*).

Visualization and Determination of the CS Tensor Orientation

According to Hansen and Bouman (*78*), a CS response surface allows for the visualization of the three-dimensional nature of the CS tensor in the molecular frame. Using spherical polar coordinates, the shielding response parallel to the applied field (i.e., the first-order secular response which causes frequency shifts in the NMR spectrum), $T_{\parallel}(\theta, \varphi)$, is
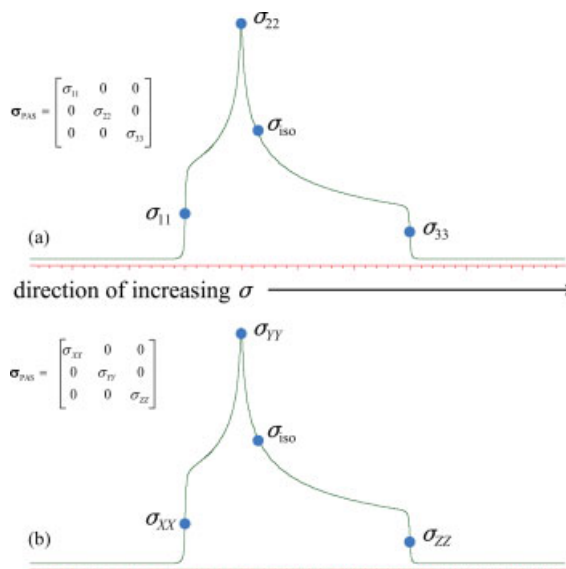

Figure 2 Comparison of the shielding tensor conventions used. (a) Principal components as per the frequency-ordered principal shift values and Maryland conventions. (b) Principal components according to the Haeberlen–Mehring–Spiess convention. [Color figure can be viewed in the online issue, which is available at www.interscience.wiley.com.]

defined as follows (a partial derivation is provided in the Appendix):

$$T_{\parallel}(\theta, \phi) = \sin^2\theta \lfloor \sigma_{xx} \cos^2\phi + \sigma_{yy} \sin^2\phi + \sigma_{xy} \sin 2\phi \rfloor$$
$$+ \sin 2\phi [\sigma_{xz} \cos\phi + \sigma_{yz} \sin\phi] + \cos^2\theta\sigma_{zz}. \quad (9)$$

A plot of the shielding response surface for one of the magnetically equivalent carbon atoms in ethene is provided in Fig. 3.

If a suitable single crystal is available, it is possible to use NMR to determine the orientation of the chemical shift tensor in the frame of the molecule. Because the principal axes of the CS and chemical shift tensors are collinear (e.g., $\boldsymbol{\sigma}_{11}$ is collinear with $\boldsymbol{\delta}_{11}$, etc.), the same methods may be used to determine the orientation of the principal axes of the CS tensor, with respect to the molecular frame or atomic coordinates (*85–93*). Generally speaking, the parameters of the *chemical shift* tensors are measured experimentally by NMR spectroscopy, whereas the *chemical shielding* tensor parameters are obtained from computational or hybrid computation/experimental techniques. For microcrystalline or amorphous/disordered samples (the more common cases and our focus herein), experimental determination of the absolute CS tensor orientation is not generally possi-
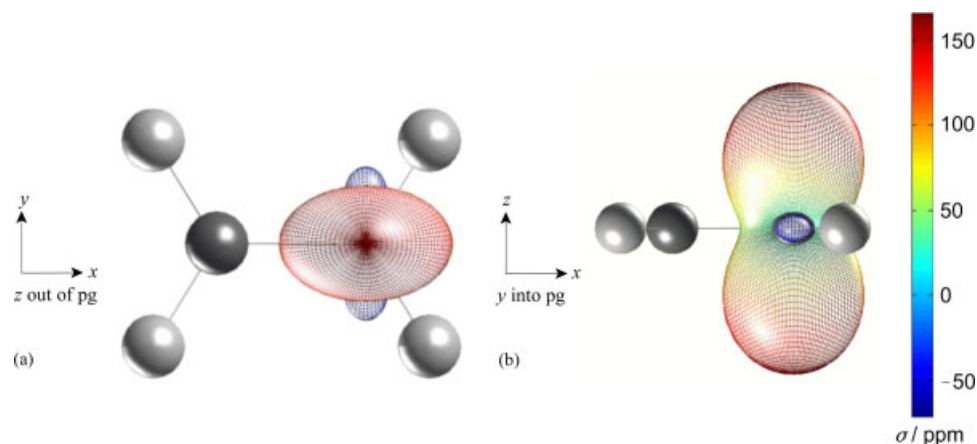
Figure 3 The symmetric first-order shielding response surface for one of the symmetry-related carbon atoms in ethene, as defined by Hansen and Bouman (*78*), (a) down the *z*-axis of the molecule and (b) down the *y*-axis of the molecule. The value of shielding along a direction is specified by colour, as defined in the scale on the right. [Color figure can be viewed in the online issue, which is available at www.interscience.wiley.com.]

ble. In many cases, it is possible to propose an orientation for the CS tensor, because the magnitude of its principal components and orientation of its axes are determined by the symmetry elements (i.e., rotational axes, mirror planes, etc.) present at the nuclear site (*76, 83, 94*). When symmetry elements are not apparent or are absent, computational techniques have been shown to be reliable in predicting the orientation of the CS tensor. These findings are confirmed by comparison with experimentally determined chemical shift tensors (using single-crystal NMR techniques (*95–97*) or separated-local-field (*73*) and chemical shift recoupling experiments (*98, 99*) for microcrystalline powder samples). A chemical shift tensor may, at the very least, be partially oriented in the molecular frame if the system of interest consists of two isolated spin-1/2 nuclides that are dipolar-coupled (*100–104*).

Diamagnetic and Paramagnetic Shielding

Ramsey's general theory of magnetic shielding arbitrarily decomposes shielding contributions into diamagnetic, $\ddot{\sigma}^d$, and paramagnetic, $\ddot{\sigma}^p$, portions, such that $\ddot{\sigma} = \ddot{\sigma}^d + \ddot{\sigma}^p$, which are dependent on the orbital angular momentum of the electron (*3*). Diamagnetic shielding results from the applied magnetic field, $\mathbf{B}_0$, inducing circulation of electrons, which in turn induce a small magnetic field opposing the applied magnetic field at the nucleus. As contributions are from the ground-state wave function only, the diamagnetic contribution to CS (or Lamb term) is readily calculated in many cases (*15, 22*):

$$\sigma_{ij}^d = \frac{e^2\mu_0}{8\pi m_e} \langle\psi_0| \sum_k \frac{\mathbf{r}_k \cdot \mathbf{r}_{kN}\, \delta_{ij}^K - r_{kNi}\, r_{kNj}}{r_{kN}^3} |\psi_0\rangle$$
$$i,j = x,y,z, \quad (10)$$

where σ_{ij}^d is element *ij* of a diamagnetic shielding tensor, ψ_0 is a ground-state wave function, δ_{ij}^K is the Krönecker delta function and $\mathbf{r}_{kN}$ is the distance of electron *k* relative to nucleus *N*. Contributions of all *k* electrons are considered, the equation is in MKS units and the origin of the magnetic vector potential (i.e., the gauge origin) is taken to be at the nucleus of interest.

The paramagnetic contribution is also induced by the application of $\mathbf{B}_0$, and arises from the mixing of the ground state with various excited states. The calculation of $\ddot{\sigma}^p$ is considerably more complicated than $\ddot{\sigma}^d$, because the former relies on highly accurate descriptions of excited electronic state wave functions:

$$\sigma_{ij}^p = -\frac{e^2\mu_0}{8\pi m_e^2} \sum_n \frac{1}{E_n - E_0}$$
$$\times \left[\langle\psi_0| \sum_k \hat{L}_{ki} |\psi_n\rangle \langle\psi_n| \sum_k \frac{\hat{L}_{kNj}}{r_{kN}^3} |\psi_0\rangle + \text{c.c.} \right] \quad (11)$$

where σ_{ij}^p is element *ij* of the paramagnetic shielding tensor, E_n and E_0 are the eigenvalues associated with an excited and the ground electronic state, respectively, $\hat{L}_{ki}$ and $\hat{L}_{kNj}$ are angular momentum operators with respect to the magnetic field and nuclear origins, respectively, and c.c. represents the complex conjugate. A summation is made over all electrons and
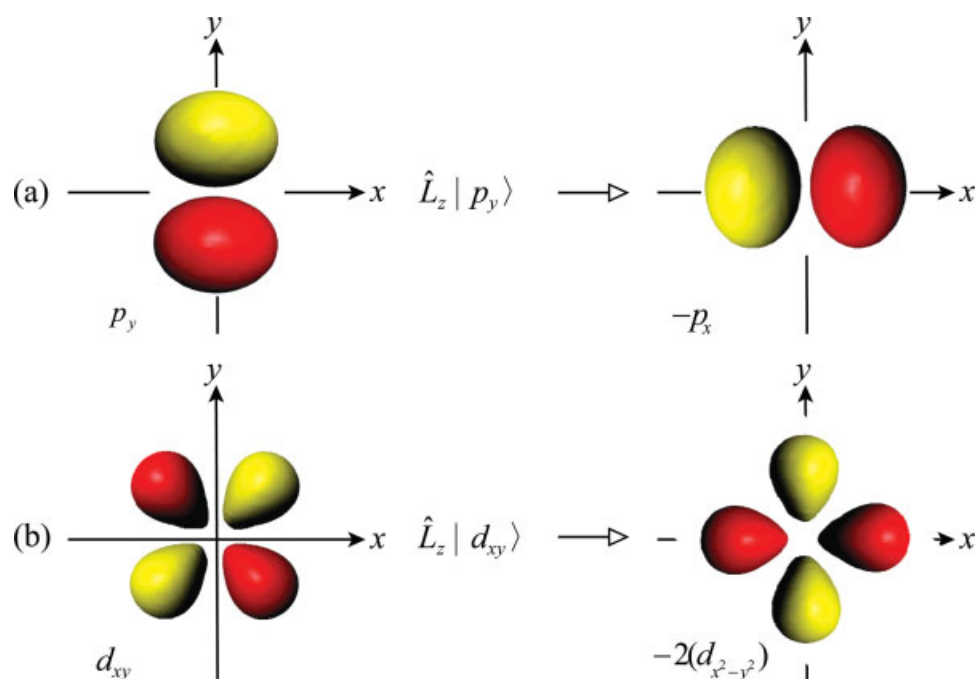
Figure 4 When $\hat{L}_z$ operates upon the (a) p_y and (b) d_{xy} AOs, they are transformed into other AOs, or more generally, a linear combination of other AOs. These transformations can be visualized as counterclockwise rotations of the AOs about the positive z-axis. [Color figure can be viewed in the online issue, which is available at www.interscience.wiley.com.]

electronic states to calculate the paramagnetic shielding contributions, σ_{ij}^{p}. In both [10] and [11], the integrals describe the degree of superposition (also referred to as "mixing" or "overlap") between the unaltered "bra" wave function (left) and the "ket" wave function (right) which has been altered by the corresponding operators; however, we will focus much of our discussion on understanding the integrals of the type in Eq. [11], and how the angular momentum operators mix these wave functions. The effect of the angular momentum operators upon p- and d-type AO wave functions has been described previously (Fig. 4) and the fashion in which they contribute to $\ddot{\sigma}^{\mathrm{p}}$ has been described using LCAO-MO and valence-bond (VB) theories (77).

It is critical to note that Ramsey's formulation is only suitable for the simplest of molecules. There have been numerous extensions of the original theories of Ramsey for treatment of more complex molecules using MO theory, with early examples including Pople's discussion of induced current densities (6) and general CS theory (7), Slichter's discussion of fluorine chemical shifts (105) and thorough treatment of CS and current density (106), and the later developments and applications of LCAO-MO and

VB calculations of CS parameters (45, 107). All of these methods, and many that followed, use three-centre integrals similar to those in Ramsey's original treatment, though the nature of the wavefunctions and partitioning of the various terms differ, and continue to vary in contemporary theoretical frameworks (*vide infra*).

Ramsey's Equations and Modern Computational Software

Ramsey's equations, as expressed in [10] and [11], are not employed by computational software for calculating CS parameters. For the study described herein, Amsterdam density functional (ADF) software was used to calculate the shielding parameters. ADF uses MOs that are generated from linear combinations of fragment orbitals (FOs) (108) to parameterize the electron density, according to Kohn and Sham (109), which is then used to calculate the total electronic energy. Using the calculated energy, the magnetic shielding is determined as described in Appendix B, and the total paramagnetic shielding contribution, $\ddot{\sigma}^{\mathrm{p}}$, is arbitrarily decomposed into

occupied–occupied MO (occ–occ) and occupied–virtual MO (occ–vir) portions:

$$\ddot\sigma^{\rm p} = \ddot\sigma^{\rm p}({\rm occ-occ}) + \ddot\sigma^{\rm p}({\rm occ-vir}). \qquad (12)$$

The contributions to paramagnetic shielding have been analysed according to pair-wise MO mixing several times before, although the analysis was often performed using approximate or empirical methods (110, 111), qualitative discussions (40, 112–115), or schematised representations of the MOs (116–118). More thorough treatments have tended to account for observed isotropic chemical shift values (39, 119); however, relatively few (compared with the total number of accounts of observed/calculated CS) can be found where this discussion is extended to include anisotropic CS (38, 41, 43, 48, 120, 121). A more detailed account of how the ADF software implements shielding calculations is provided in the Appendix; for full treatments, the reader is referred to the literature (51, 122–125).

Determination of Symmetry-Allowed Contributions to the Paramagnetic CS Tensor

In all forms of spectroscopy (126), three-centre integrals of the form $\int \psi_b \hat{O} \psi_a d\tau$ ($\hat{O}$ being an appropriate transition dipole moment operator) are evaluated to determine i) whether the transitions are allowed or forbidden by symmetry and ii) the probabilities (magnitudes) of the allowed transitions. Evaluation of this integral provides a measure of the interaction of the system with EM radiation, whereas its square gives the probability of the transition occurring. For optical, vibrational, and rf spectroscopies, the transition electric dipole moment operators belong to the same IRs as the translational operators, $\hat{T}_x$, $\hat{T}_y$, and $\hat{T}_z$, listed in character tables. The three-centred integrals encountered in theoretical descriptions of CS appear to have a similar form, but have completely different physical origins. Nonetheless, these integrands may be evaluated using methods encountered in most spectroscopy, symmetry, and group theory courses.

Consideration of MO symmetries aids in understanding the origins and mechanisms of CS, as well as the relationships between molecular structure and experimentally observed $\delta_{\rm CSA}$ patterns. Making use of the molecular symmetry also helps to increase the efficiency of calculations, because symmetry-forbidden contributions do not have to be explicitly eval-

uated. A pair of MOs contributes to CS if the following integral is nonzero:

$$\langle \phi_b | \hat{L}_n | \phi_a \rangle = \int \phi_b \hat{L}_n \phi_a \; d\tau \neq 0 \qquad (13)$$

where ϕ_b and ϕ_a refer to single-electron MOs and $\hat{L}_n$ is an angular momentum operator ($n = x, y, z$). The left hand side of the equation describes the integral using Dirac's bra-ket notation. The magnitude of the contributions is proportional to the MO mixing coefficient and inversely proportional to the energetic separation (ΔE) between the occupied and virtual MOs. The effect that the angular momentum operator has on a given AO or MO may be appreciated visually and appears as a simple rotation of the object about a particular axis. This "charge rotation" mechanism and illustration of the function of the angular momentum operator are shown schematically for F_2 (Fig. 5).

Depending on the symmetry at the nuclear site, one may easily determine the number of unique shielding tensor components, as outlined by Buckingham and Malm (94). Nuclei at the centre of the molecules, or contained within all of the symmetry elements, are said to have nuclear site symmetries which are the same as that of the molecule; however, nuclei positioned in other locations may have point group symmetries lower than the overall molecular symmetry, and hence, have CS tensors with very different symmetry characteristics. The angular momentum operators belong to the same IRs as the corresponding rotational operators in the appropriate symmetry group (hence, $\Gamma(\hat{L}_n) = \Gamma(\hat{R}_n)$) (45). However, there is a caveat here: the matrix elements for the external magnetic field in Ramsey's expression for paramagnetic shielding (Eq. [11]), $\langle \psi_0 | \sum_k \hat{L}_{ki} | \psi_n \rangle$, involve angular momentum operators which transform as rotational operators with the point group symmetry of the entire molecule, regardless of the nuclear site symmetry. However, the matrix elements for the nuclear spin, $\langle \psi_n | \sum_k \hat{L}_{kNj} / r_{kN}^3 | \psi_0 \rangle$, include angular momentum operators which are dependent upon the local nuclear point group symmetry; hence, only sites where the nucleus is in a local symmetry adapted coordinate origin (i.e., the nuclear site symmetry is the same as that of the molecule) may be evaluated by the methods outlined latter for this term. In this article, we consider only evaluations of the former term for nuclear sites with point group symmetries matching that of the molecule. We note that it is possible to apply this analysis to nuclei in sites of lower point group symmetries, provided that appropriate symme-
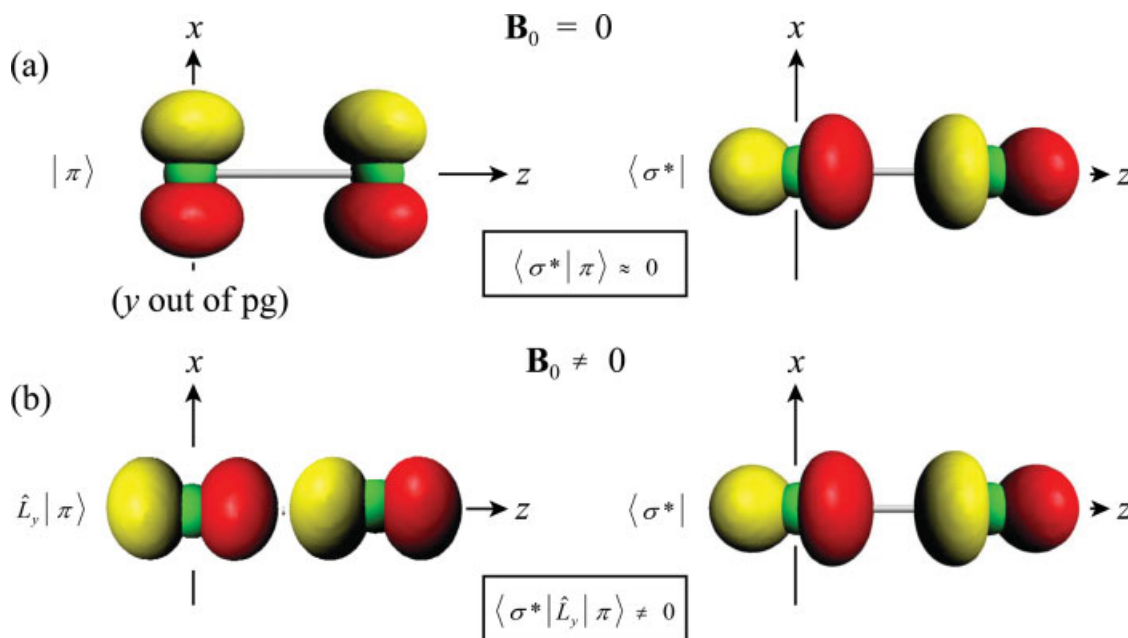
Figure 5 According to earlier reports (*51*), $\pi \leftrightarrow \sigma^*$ (mixing) makes the most significant contribution to the paramagnetic shielding tensor of the F_2 molecule. Before the application of $\mathbf{B}_0$ (a), the orbitals do not possess the correct symmetry to overlap either constructively or destructively and do not contribute to the paramagnetic shielding tensor; however, after application of $\mathbf{B}_0$ (b), induced electron circulation results in nonzero orbital overlap and a contribution to shielding. [Color figure can be viewed in the online issue, which is available at www.interscience.wiley.com.]

try adapted linear combinations of nuclear sites and components of this operator are used.

Therefore, in a fashion analogous to using translational operators for the evaluation of transitions in optical spectroscopy, angular momentum operators will be used to determine if MO pairs have the appropriate symmetry to have nonzero overlap and potentially contribute to $\ddot{\sigma}^p$. Evaluation of [**13**] is simplified considerably by considering the direct product of the symmetry representations of the MOs and rotational operators. If the direct product equals or contains the totally symmetric representation (*A*) (Note that the totally symmetric representation can be *A*, A', A_g, A_{1g}, etc.) of a given point group, i.e.,

$$\Gamma(\phi_b) \otimes \Gamma(\hat{R}_n) \otimes \Gamma(\phi_a) \supseteq A \qquad (14)$$

then the integral is nonzero and the contribution to $\ddot{\sigma}^p$ is said to be symmetry-allowed (*46*). In certain high-symmetry cases, the axis of the rotational operator will correspond to the orientation of a principal axis of the CS tensor. It is stressed that the evaluation of [**14**] does not offer insight into the magnitude of the contribution to $\ddot{\sigma}^p$, but rather only if the contribution is *allowed by symmetry*. It does not address

instances where the integral is zero for reasons other than symmetry (*vide infra*); however, this methodology provides a basis that one may use to predict the orientation of an observed chemical shift tensor, or rationalize the origins of a calculated shielding tensor.

METHODOLOGY

Geometry optimizations were conducted using the self-consistent field method as implemented in the ADF program, version 2005.01 (*108*, *127*, *128*), distributed by Scientific Computing and Modelling. NMR CS calculations were carried out using the NMR (*51*, *123*, *124*) and EPR (*129*) modules. Both modules use the GIAO method to account for the gauge variance encountered when using finite basis sets. DZ and TZ2P all-electron basis sets were used on all atoms, with values reported herein originating from calculations using the TZ2P basis. The DZ basis set is nonrelativistic, double-ζ in the valence, whereas the TZ2P basis is nonrelativistic, triple-ζ in the valence with two polarization functions; both ba-

Table 1 C_2H_4: Contributions to Carbon Chemical Shielding (ppm)[a]

Contribution	σ_{11} (ppm)	σ_{22} (ppm)	σ_{33} (ppm)	σ_{iso} (ppm)	Ω (ppm)	$\Delta\sigma$[b] (ppm)	κ
σ^d (Total)	247.32	247.26	216.43	237.00	–	–	–
σ^p (Gauge)	0.00	0.00	–8.90	–2.97	–	–	–
σ^p (occ–occ)	47.80	80.98	192.65	107.14	–	–	–
σ^p (occ–vir)	–366.31	–267.90	–234.18	–289.47	–	–	–
σ^p (Total)	–318.51	–186.92	–50.44	–185.29	–	–	–
σ (Total)	–71.19	60.34	165.99	51.71	237.18	184.36	–0.11
Experiment (112, 132, 133)	–	–	–	63.3[c]	210	162	–0.09
Calculation (134)	–	–	–	74.76[d]	–	–	–
Calculation (135)	–	–	–	60.89[e]	–	–	–

[a] TZ2P all-electron basis set on all atoms, see theoretical section for parameter definitions.
[b] The anisotropy will assume a negative value only if σ_{zz} is to low frequency of σ_{iso}.
[c] Average reported value.
[d] Hartree-Fock (HF) approximation at equilibrium geometry.
[e] HF approximation, zero-point vibrationally corrected value.

sis sets are double-ζ in the core. All DFT calculations used Becke's exchange functional (130) and the correlation functional proposed by Lee et al. (131) (BLYP). Optimized geometries using the two different basis sets are provided in the Supporting Information (Table S1).

RESULTS AND DISCUSSION

Preamble

The approach outlined earlier is first applied to several model systems, followed by analysis of a few relevant cases from the literature. Key data is summarized in tables within the article, and supplementary data tables are included in the Supporting Information. Several reasons motivated the choice of each model system. First, each molecule was chosen to be relatively small (i.e., at most perhaps 10 atoms), allowing for rapid computation of the CS tensors and production of manageable datasets for analysis and discussion. Second, systems were also chosen where relativistic effects on CS, which greatly complicate the presentation of the analysis, can be safely ignored. Third, it was ensured that experimental chemical shift tensor information is available for each system, allowing for comparisons between calculated and experimental parameters, and easy assessment of the success of the theoretical model. Finally, molecules were chosen with several different nuclear site symmetries, to demonstrate the wide applicability of the model, and reveal any potential issues with treating certain symmetry groups. To this end, we chose at least one case where the nuclear site

possessed nondegenerate, doubly degenerate or infinitely degenerate rotational symmetry axes.

Ethene, C_2H_4

Isotropic Carbon CS. The isotropic carbon CS value ($\sigma_{iso}(^{13}C)$) of a geometry-optimized C_2H_4 molecule (see Supporting Information Table S1 for geometry) is calculated to be 51.71 ppm (Table 1). This value is in fair agreement with previous reports, based on gas phase (132, 133) ($\sigma_{iso}(^{13}C) = 64.5$ ppm) and low-temperature solid-state (112) ($\sigma_{iso}(^{13}C) = 62.1$ ppm) measurements. When using DFT methods to calculate isotropic CS, it has been found that calculated shielding values are often deshielded relative to those which have been experimentally observed. It has also been established that the largest discrepancies occur when the molecule has a very large isotropic σ^p value. Chesnut proposes the following semiempirical relationship to address this issue (136):

$$\ddot{\sigma}' = \ddot{\sigma}^d + k\ddot{\sigma}^p \qquad (15)$$

where k is an empirically determined scaling factor, equal to 0.952 for carbon. The diamagnetic and paramagnetic shielding values are calculated to be 237.00 ppm and –185.29 ppm, respectively (Table 1). Application of [15] results in a scaled isotropic carbon shielding value, σ'_{iso}, of 60.60 ppm, in better agreement with the experimental values. It is also clear that occ–vir MO mixing contributes more significantly to σ^p than does occ–occ MO mixing.

Anisotropic Carbon CS. Low-temperature ssNMR measurements of carbon δ_{CSA} in ethene highlight a
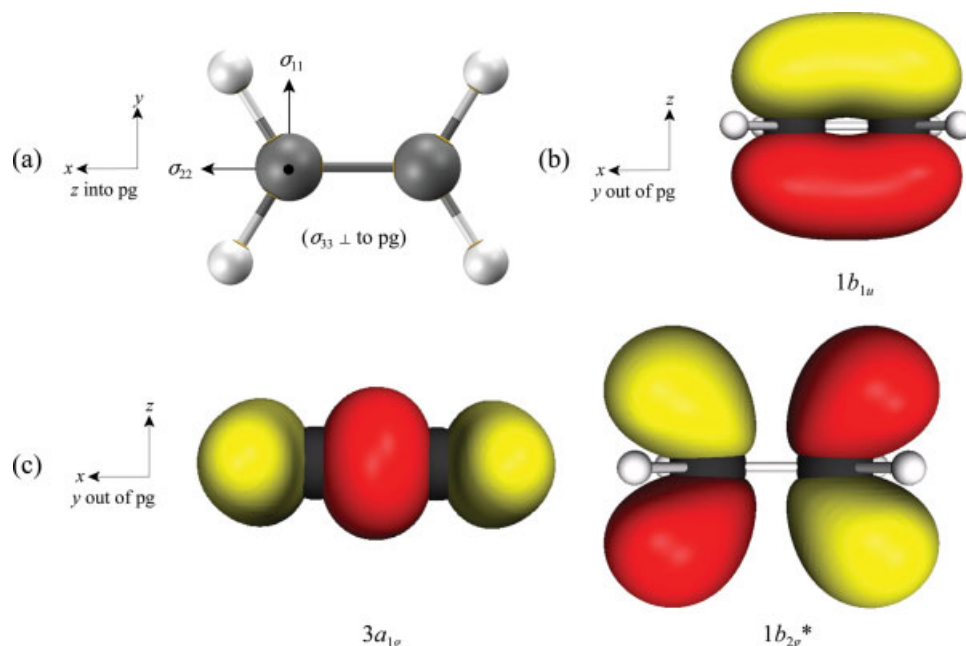
Figure 6 (a) Carbon chemical shielding tensor orientation for ethene. (b) The $1b_{1u}$ MO is of high p_z AO character and contributes to the diamagnetic shielding tensor in an anisotropic fashion (red represents negative contours, yellow represents positive). (c) An example of symmetry-allowed MO mixing is provided by considering $3a_{1g} \leftrightarrow 1b_{2g}*$ ($\leftrightarrow$ denotes MO mixing). The $\hat{L}_y$ operator transforms the $3a_{1g}$ MO such that it will have nonzero overlap with the $1b_{2g}*$ MO. To visualize, imagine the $3a_{1g}$ MO being rotated about the y-axis, but with the origin at the nuclear site. As the orbitals overlap out-of-phase with one another and the rotation was performed about the y-axis, chemical deshielding will result and it will be parallel to the y-axis (along $\boldsymbol{\sigma}_{11}$). [Color figure can be viewed in the online issue, which is available at www.interscience.wiley.com.]

large, nonaxially symmetric shift tensor ($\Omega(^{13}C) = 210$ ppm; $\kappa(^{13}C) = -0.09$) (*112*). The calculated carbon CS tensor parameters are in reasonable agreement with these values, particularly the calculated value for the skew: $\Omega(^{13}C) = 237.18$ ppm; $\kappa(^{13}C) = -0.11$. The total diamagnetic carbon CS tensor (Table 1) is found to be substantially less anisotropic than the total paramagnetic carbon CS tensor. The reasons for this considerable difference depend strongly upon the origins of the contributions to $\ddot{\sigma}^d$ and $\ddot{\sigma}^p$, as discussed latter.

Ethene can be represented using the D_{2h} point group (see Supporting Information Table S2 for the character table), and, as expected, the principal components and axes of the shielding tensor depend on the symmetry of the molecule [Fig. 6(a)]. $\boldsymbol{\sigma}_{33}$ points out of the molecular plane (parallel to one of the C_2 axes of the molecule), $\boldsymbol{\sigma}_{22}$ is directed parallel to the olefinic carbon–carbon bond (along another C_2 axis) and $\boldsymbol{\sigma}_{11}$ lies perpendicular to the double bond (parallel to the direction of the third C_2 axis). This orientation agrees with previous accounts and is equivalent for both of the carbon nuclei (*137*).

Diamagnetic shielding at the carbon nucleus is largely the result of MOs dominated by large contributions from carbon AOs (see Supporting Information Table S3 for FO contributions to the MOs). It is worth noting that essentially all (ca. 98%) of the diamagnetic shielding arises from 4 MOs (Table 2). The low energy $1a_{1g}$ and $1b_{3u}$ MOs contribute to shielding in an almost isotropic manner because of their high s-character. This is because the $1a_{1g}$ and $1b_{3u}$ MOs are formed from linear combinations of the $1s$ AOs on the two carbon atoms:

$$1a_{1g} : \frac{1}{\sqrt{2}}[1s(C_1) + 1s(C_2)]$$

$$1b_{3u} : \frac{1}{\sqrt{2}}[1s(C_1) - 1s(C_2)].$$

Increasingly anisotropic contributions to $\ddot{\sigma}^d$ are due to MOs which have lower s-character. For example, the $1b_{1u}$ MO [Fig. 6(b)] is primarily a linear combination of the $2p_z$ AOs on the carbon atoms and it possesses the largest difference between principal

Table 2   C₂H₄: Significant Diamagnetic Contributions to $\ddot{\sigma}$, Arranged by MO

φ_p[a]	MO	σ_{11} (ppm)	σ_{22} (ppm)	σ_{33} (ppm)	σ_{iso} (ppm)	Δ_{pc}[b] (ppm)	s char. (%)	p char. (%)
1	$1a_{1g}$	100.1	100.2	100.1	100.1	0.1	100.0	0.0
2	$1b_{3u}$	100.1	100.3	100.1	100.1	0.2	100.0	0.0
3	$2a_{1g}$	16.0	18.0	15.3	16.4	2.7	88.0	12.0
8	$1b_{1u}$	22.8	19.2	9.6	17.2	13.2	0.0	100.0
–	rem[c]	8.3	9.6	−8.7	3.2	–	–	–

[a] Wave functions are numbered according to increasing energy, with 1 representing the lowest energy eigenstate.

[b] The value of the greatest difference between principal component values.

[c] Remaining contributions from all other MOs.

component values out of the four MOs which contribute most significantly to $\ddot{\sigma}^d$.

Contributions to $\ddot{\sigma}^p$ are largely due to occ–vir MO mixing, with $3a_{1g} \leftrightarrow 1b_{2g}^*$ and $1b_{1g} \leftrightarrow 1b_{2g}^*$ MO pairs ($\leftrightarrow$ denotes a pair of MOs that are mixing) making the most significant contributions (Table 3). According to calculation, $3a_{1g} \leftrightarrow 1b_{2g}^*$ MO mixing leads to paramagnetic deshielding along the y-axis (parallel to $\boldsymbol{\sigma}_{11}$). Three nondegenerate rotational operators are available in the D_{2h} point group, where $\Gamma(\hat{R}_x) = B_{3g}$, $\Gamma(\hat{R}_y) = B_{2g}$ and $\Gamma(\hat{R}_z) = B_{1g}$. Keeping in mind that the angular momentum operators belong to the same IRs as these rotational operators, the direct product evaluates as follows:

$$\Gamma(\phi_b) \otimes \Gamma(\hat{R}_n) \otimes \Gamma(\phi_a) = B_{2g} \otimes \begin{bmatrix} \Gamma(\hat{R}_x) \\ \Gamma(\hat{R}_y) \\ \Gamma(\hat{R}_z) \end{bmatrix} \otimes A_{1g}$$

$$= B_{2g} \otimes \begin{bmatrix} B_{3g} \\ B_{2g} \\ B_{1g} \end{bmatrix} \otimes A_{1g} = \begin{bmatrix} B_{1g} \\ A_{1g} \\ B_{3g} \end{bmatrix}. \quad (16)$$

From [**16**], it is clear that only $\hat{L}_y$ possesses the symmetry that is required to generate nonzero overlap between the MOs. This is because only this matrix element equals or contains the totally symmetric representation of the D_{2h} point group (i.e., A_{1g}). By

Table 3   C₂H₄: Significant Paramagnetic Contributions to $\ddot{\sigma}$, Arranged by MO

φ_a[a]	MO	φ_b	MO	σ_{11} (ppm)	σ_{22} (ppm)	σ_{33} (ppm)	σ_{iso} (ppm)	$\langle\varphi_b|R_n|\varphi_a\rangle$[b]
Occupied–Occupied molecular orbital mixing contributions								
4	$2b_{3u}$	5	$1b_{2u}$	0.0	0.0	76.7	25.6	$\langle b_{2u}|R_z|b_{3u}\rangle$
4		8	$1b_{1u}$	47.5	0.0	0.0	15.8	$\langle b_{1u}|R_y|b_{3u}\rangle$
5	$1b_{2u}$	8	$1b_{1u}$	0.0	81.0	0.0	27.0	$\langle b_{1u}|R_x|b_{2u}\rangle$
6	$3a_{1g}$	7	$1b_{1g}$	0.0	0.0	122.3	40.8	$\langle b_{1g}|R_z|a_{1g}\rangle$
–	–	–	rem[b]	0.3	0.0	−6.4	−2.1	–
Occupied–Virtual molecular orbital mixing contributions								
5	$1b_{2u}$	15	$2b_{1u}^*$	0.0	−38.3	0.0	−12.8	$\langle b_{1u}|R_x|b_{2u}\rangle$
5		24	$6b_{3u}^*$	0.0	0.0	−37.0	−12.3	$\langle b_{3u}|R_z|b_{2u}\rangle$
6	$3a_{1g}$	9	$1b_{2g}^*$	−219.4	0.0	0.0	−73.1	$\langle b_{2g}|R_y|a_{1g}\rangle$
6		19	$2b_{2g}^*$	−46.9	0.0	0.0	−15.6	$\langle b_{2g}|R_y|a_{1g}\rangle$
6		23	$3b_{1g}^*$	0.0	0.0	−28.5	−9.5	$\langle b_{1g}|R_z|a_{1g}\rangle$
7	$1b_{1g}$	9	$1b_{2g}^*$	0.0	−126.3	0.0	−42.1	$\langle b_{2g}|R_x|b_{1g}\rangle$
7		10	$4a_{1g}^*$	0.0	0.0	−31.2	−10.4	$\langle a_{1g}|R_z|b_{1g}\rangle$
7		18	$6a_{1g}^*$	0.0	0.0	−36.0	−12.0	$\langle a_{1g}|R_z|b_{1g}\rangle$
7		19	$2b_{2g}^*$	0.0	−47.5	0.0	−15.8	$\langle b_{2g}|R_x|b_{1g}\rangle$
–	–	–	rem[c]	−100.0	−55.8	−101.5	−85.9	–

[a] Wave functions are numbered according to increasing energy, with 1 representing the lowest energy eigenstate.

[b] Integrands which evaluate to nonzero matrix elements. To confirm MO mixing is symmetry-allowed, evaluate the direct product of the symmetry representations of the MOs and rotational operator. For brevity, the operator caret symbol has been dropped when denoting rotational operators in tables.

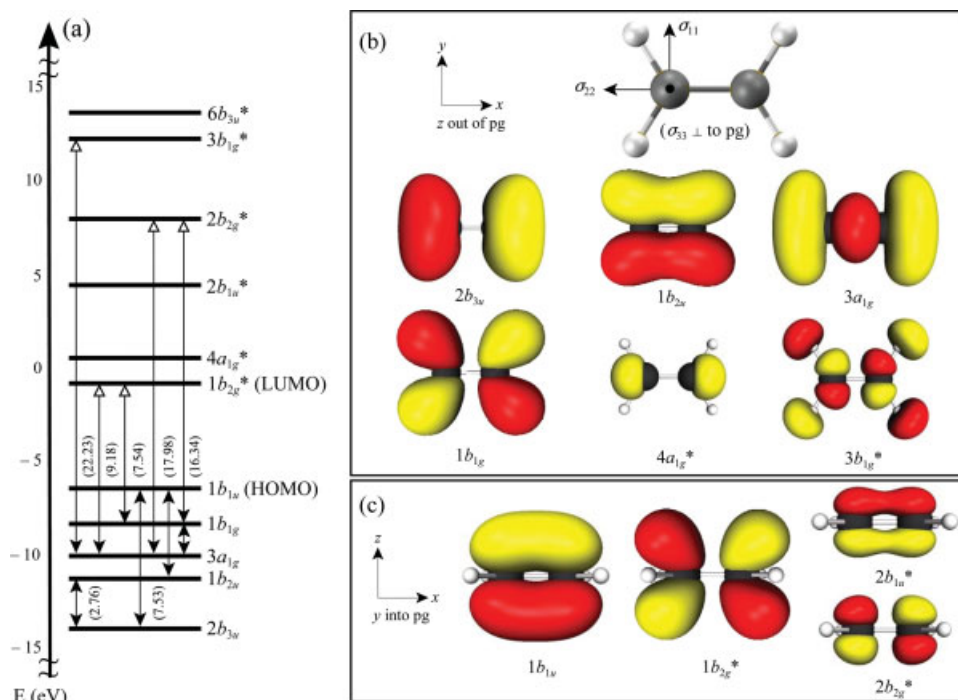[c] Remaining contributions from all other MOs.

Figure 7 (a) Partial MO diagram for ethene, highlighting MOs that make significant contributions to the paramagnetic shielding tensor (ΔE values in parentheses; open and closed arrowheads refer to virtual and occupied MOs, respectively). (b, c) Visual representations of MOs which contribute substantially to the paramagnetic shielding tensor, as viewed along the z (b) and y (c) directions. [Color figure can be viewed in the online issue, which is available at www.interscience.wiley.com.]

observing the orientation of the CS tensor in the frame of the molecule [Fig. 6(a)], it is seen that y and $\boldsymbol{\sigma}_{11}$ are collinear. Hence, $3a_{1g} \leftrightarrow 1b_{2g}*$ is symmetry-allowed and must produce shielding along $\boldsymbol{\sigma}_{11}$, in agreement with the ADF calculated direction. To determine the magnitude of the shielding that is produced by this MO pair, two important factors must be considered, including the degree of overlap between the two MOs and their separation in energy (ΔE). The overlap between the MO pairs can be qualitatively visualized as the result of a rotation of one of the MOs [Fig. 6(c)]. By performing a positive (counterclockwise) rotational transformation on the $3a_{1g}$ MO about the y-axis (with the y-axis passing through either carbon), a high degree of overlap with the $1b_{2g}*$ MO results. The MO overlap is destructive (i.e., for this example, red and yellow lobes overlap), which corresponds to a negative contribution to shielding (i.e., deshielding). If constructive overlap is observed (i.e., red overlaps with red, yellow with yellow), the result is a positive shielding contribution. Finally, it is seen that these two MOs are relatively close in energy [$\Delta E = 9.18$ eV, Fig. 7(a)]. Generally speaking, important occ–vir contributions in a system

with a closely spaced HOMO and LUMO, such as a conjugated carbon system, commonly involve these MOs or other MOs which are energetically similar (e.g., HOMO+1, LUMO-2, etc).

If the same procedure is applied to predict the direction of the deshielding produced by the $1b_{1g} \leftrightarrow 1b_{2g}*$ MO pair, it is clear that the symmetry of the angular momentum operator must belong to the B_{3g} IR. Hence, the deshielding produced by this MO pair is along the x-axis of the molecule, which is coincident with $\boldsymbol{\sigma}_{22}$ (Table 3). Additional contributions to $\ddot{\sigma}^{\mathrm{p}}$ exist (see Fig. 7 for a schematic of the important eigenstates, and ADFview (138) renderings of a number of the MOs which contribute substantially to $\ddot{\sigma}^{\mathrm{p}}$), but they largely cancel one another out. It is clear that the $3a_{1g} \leftrightarrow 1b_{2g}*$ and $1b_{1g} \leftrightarrow 1b_{2g}*$ MO pairs are responsible to a great extent for the resultant span and skew values of the carbon CS tensor. Other MO pairs contribute more modestly to $\ddot{\sigma}^{\mathrm{p}}$, due in large part to: i) larger separation in energies, ΔE and ii) while the occupied orbitals are typically of high carbon character, a number of the virtual orbitals have significant hydrogen character (see Supporting Information Table S3), and do not lead to significant

Table 4   HF: Contributions to Fluorine Chemical Shielding (ppm)[a]

Contribution	σ_{11} (ppm)	σ_{22} (ppm)	σ_{33} (ppm)	σ_{iso} (ppm)	Ω (ppm)	$\Delta\sigma$ (ppm)	κ
σ^d (Total)	465.08	465.08	481.51	470.56	–	–	–
σ^p (Gauge)	0.00	0.00	0.00	0.00	–	–	–
σ^p (occ–occ)	106.03	106.03	0.00	70.69	–	–	–
σ^p (occ–vir)	−205.84	−205.84	0.00	−137.23	–	–	–
σ^p (Total)	−99.81	−99.81	0.00	−66.54	–	–	–
σ (Total)	365.27	365.27	481.51	404.02	116.24	−116.24	1.00
Experiment (139, 144)	–	–	–	410 ± 6	108 ± 9	−108 ± 9	1.00
Calculation[b] (140–142)	–	–	–	418.4[c]	–	–	–

[a] TZ2P all-electron basis set on all atoms, see theoretical section for parameter definitions.
[b] Results from high-level calculations.
[c] Average calculated value.

shielding contributions at the carbon nuclei (i.e., relatively small overlap coefficient magnitudes).

Hydrogen Fluoride, HF

Isotropic Fluorine CS.   Using a geometry-optimized HF molecule (see Supporting Information Table S1 for geometry), $\sigma_{iso}(^{19}F)$ is calculated to be 404.02 ppm (Table 4), in relatively good agreement with the hybrid computational-experimental value determined for the gas-phase molecule ($\sigma_{iso}(^{19}F)$ = 410 ± 6 ppm) (139). In fact, the presently calculated value is as close to this value of σ_{iso} as high-level coupled-cluster (CCSD(T)) (140) and relativistic Hartree-Fock (141, 142) calculations. This is in line with earlier conclusions that electron-correlation and relativistic effects are not very significant in this molecule, each making maximal contributions to $\sigma_{iso}(^{19}F)$ of about 5 ppm (143). In contrast to ethene, diamagnetic contributions dominate the CS tensor, with the total contributions to the isotropic portions of $\ddot{\sigma}^d$ and $\ddot{\sigma}^p$ equalling 470.56 ppm and –66.54 ppm, respectively. Because of the small magnitude of $\ddot{\sigma}^p$, a scaling calculation is not warranted.

Anisotropic Fluorine CS.   There do not appear to be any reports in the literature regarding the direct measurement of fluorine shielding anisotropy in a ground-state HF molecule using NMR spectroscopy. High-resolution molecular-beam electron-resonance measurements taken from an excited state ($v = 0$, $J = 1$) HF molecule reveal an axially symmetric ($\kappa(^{19}F) = +1.00$) fluorine CS tensor with significant anisotropy in fluorine shielding when comparing directions perpendicular and parallel to the HF bond axis ($\Omega(^{19}F) = 108 ± 9$ ppm) (144). It has been established that the shielding tensor differences between the ground- and first-excited rotational states

are minimal, on the order of 0.1 ppm (145). DFT calculations reported herein agree reasonably well with the previous account ($\Omega(^{19}F) = 116.24$ ppm; $\kappa(^{19}F) = +1.00$; Table 4).

The fluorine shielding tensor elements of HF ($C_{\infty v}$ symmetry, see Supporting Information Table S4 for character table) are determined by the symmetry of the molecule: $\boldsymbol{\sigma}_{33}$ is along the bonding and C_{∞} rotational axis, whereas $\boldsymbol{\sigma}_{11}$ and $\boldsymbol{\sigma}_{22}$ are perpendicular to this axis (Fig. 8). Because of the axial symmetry of HF, and by extension, the shielding tensor, σ_{11} and σ_{22} are equivalent; hence, their labels may be interchanged and they are collectively referred to as $\sigma_\perp$, as they are perpendicular to the HF bonding axis (as well, σ_{33} may be denoted as $\sigma_\parallel$).

The diamagnetic contributions to fluorine CS (Table 5) share many of the traits that were observed in the $\ddot{\sigma}^d$ contributions in ethene. The largest contributions are due to the angular momentum expectation values in low-lying MOs (1σ, 2σ, etc.; the five MOs in Table 5 account for 100% of the calculated $\ddot{\sigma}^d$), they are considerably less anisotropic than $\ddot{\sigma}^p$ components, and the contributions become less isotropic as the degree of MO s character is decreased (see Supporting Information Table S5 for FO contributions to the HF MOs).

The fluorine paramagnetic shielding tensor does not have any significant contributions that arise from MO mixing due to $\hat{L}_z$ (in fact, there are not even trace contributions due to $\hat{L}_z$, Table 6). Because of this, paramagnetic deshielding is not observed along this axis and it becomes clear that $\boldsymbol{\sigma}_{33}$ should be oriented parallel to this direction. Using group theory, it is easy to see why this is: In Table 6, it is seen that only $\sigma \leftrightarrow \pi$ overlap contributes substantially to $\ddot{\sigma}^p$. The $1\pi \leftrightarrow 6\sigma^*$ MO pair (MO renderings are provided in Fig. 8) serve as the example. First, one notes that in addition to the $\hat{L}_z$ operator [$\Gamma(\hat{L}_z) = \Gamma(\hat{R}_z) = A_2$], the
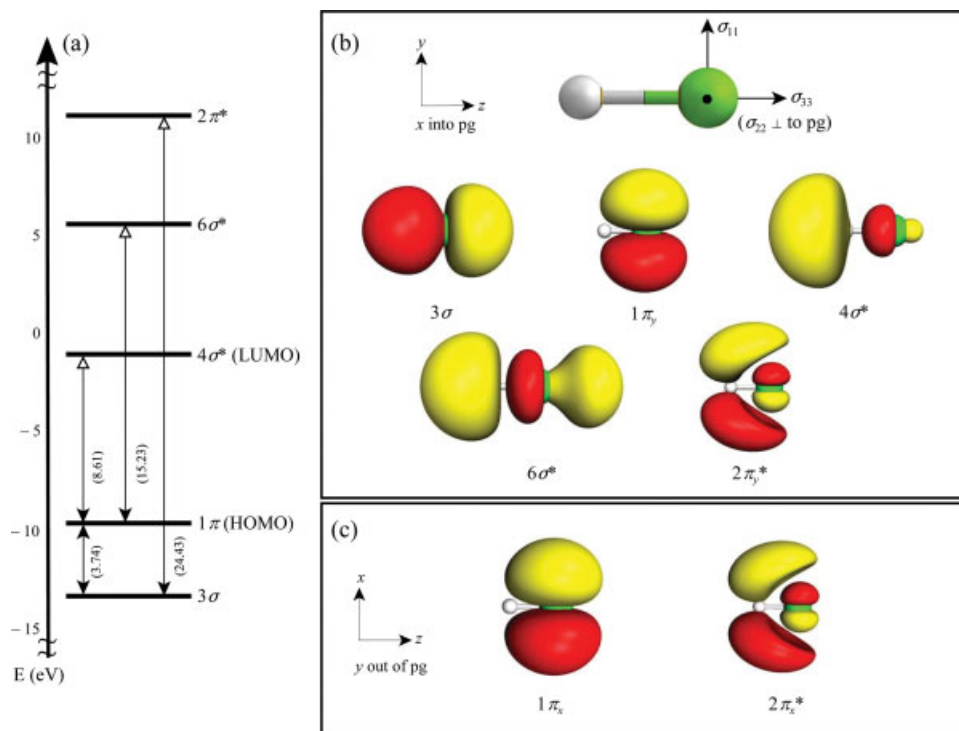
Figure 8 (a) Partial MO diagram for HF, highlighting MOs that make significant contributions to the paramagnetic shielding tensor (ΔE values in parentheses). (b, c) Fluorine chemical shielding tensor orientation for HF in the molecular frame (top) along with visual representations of the MOs which contribute substantially to the paramagnetic shielding tensor, as viewed along the x (b) and y (c) directions. [Color figure can be viewed in the online issue, which is available at www.interscience.wiley.com.]

$C_{\infty v}$ point group possesses a doubly degenerate rotational operator $(\hat{R}_x, \hat{R}_y)$ which belongs to the E_1 representation. The direct product of the symmetry representations for the $1\pi \leftrightarrow 6\sigma^*$ MO pair evaluates as:

$$\Gamma(\phi_b) \otimes \Gamma(\hat{R}_n) \otimes \Gamma(\phi_a) = A_1 \otimes \begin{bmatrix} E_1 \\ A_2 \end{bmatrix} \otimes E_1$$

$$= \begin{bmatrix} A_1 + A_2 + E_2 \\ E_1 \end{bmatrix}. \quad (17)$$

From [**17**], the σ and π MOs undergo symmetry-allowed mixing only when the angular momentum operator may be represented by E_1, (recall that the degenerate angular momentum operators belong to the same IR as $(\hat{R}_x, \hat{R}_y)$). Conversely, the $\hat{L}_z$ operator does not possess the correct symmetry to mix any of these types of MOs; therefore, there can be no resultant shielding along this direction, as predicted in the calculations. This ensures that the $\boldsymbol{\sigma}_{33}$ component of the shielding tensor points along the C_∞ axis.

Because each π MO can be broken into orthogonal π_x and π_y components, when they mix with a σ MO (i.e., $\sigma \leftrightarrow \pi_x$ and $\sigma \leftrightarrow \pi_y$), their contributions to

shielding are equal, as both orbital overlaps and ΔE values for each direction are identical. Thus, the fluorine CS tensor must be axially symmetric. Again, the degree to which each MO pair contributes to shielding is typically most pronounced when the energy difference, ΔE, between the mixing MOs is small. It is observed that the most significant paramagnetic contributions to CS are due to the 1π (HOMO), the $4\sigma^*$ (LUMO), and a few other energetically similar MOs (i.e., 3σ, $2\pi^*$, $6\sigma^*$).

Trifluorophosphine, PF₃

Isotropic Phosphorus CS. The isotropic CS value at the ^{31}P nucleus in a geometry-optimized PF₃ molecule (see Supporting Information Table S1 for geometry), $\sigma_{\text{iso}}(^{31}\text{P})$, was calculated to be 153.65 ppm (Table 7), clearly in poor agreement with the experimental value of 222.69 ppm reported by Jameson (*10*). In contrast to HF, the phosphorus paramagnetic shielding term is of considerable magnitude ($\sigma_{\text{iso}}^{\text{p}} = -803.20$ ppm) and therefore a scaling calculation is performed. The empirical scaling factor for

Table 5 HF: Significant Diamagnetic Contributions to $\ddot{\sigma}$, Arranged by MO

φ_p	MO	σ_{11} (ppm)	σ_{22} (ppm)	σ_{33} (ppm)	σ_{iso} (ppm)	Δ_{pc} (ppm)	s char. (%)	p char. (%)
1	1σ	305.8	305.8	305.8	305.8	0.0	100.0	0.0
2	2σ	47.9	47.9	46.9	47.6	1.0	95.6	4.4
3	3σ	32.2	32.2	24.6	29.6	7.6	77.4	22.6
4	$1\pi_x$	52.9	26.3	52.1	43.8	26.6	0.0	100.0
5	$1\pi_y$	26.3	52.9	52.1	43.8	26.6	0.0	100.0
–	rem	0.0	0.0	0.0	0.0	–	–	–

phosphorus was determined to be 0.906 ± 0.008, yielding $\sigma'_{iso}(^{31}P)$ = 229.15 ppm, in good agreement with both the experimental findings as well as high-level CCSD(T) calculations (148). In contrast to the CS values provided earlier for ethene and HF, contributions to $\ddot{\sigma}^p$ at the phosphorus atom in PF_3 are dominated by occ–vir mixing to the point where occ–occ mixing is of minor significance.

Anisotropic Phosphorus CS. ^{31}P NMR measurements of PF_3 highlight a very anisotropic shielding environment, with $\Omega(^{31}P)$ ranging from 181 ± 5 ppm to 228 ± 2 ppm when dissolved in smectic (146) and nematic (147) liquid crystal solvents, respectively. This span, which represents a significant fraction of the total phosphorus shielding range (currently reported as ca. 1500 ppm for diamagnetic samples) (149), is confirmed by the calculations reported herein, as $\Omega(^{31}P)$ = 247.97 ppm (Table 7). All previous experimental observations and theoretical treatments report an axially symmetric phosphorus shielding tensor ($\kappa(^{31}P)$ = +1.00), in agreement with our calculations.

PF_3 has C_{3v} symmetry (Supporting Information Table S6), and as with ethene and HF, the orientation of the shielding tensor [Fig. 9(a)] is determined by its symmetry elements: because the CS tensor is axially symmetric with σ_{33} as the unique component (κ = 1.0), it is of no surprise that σ_{33} lies along the C_3 axis (z-direction), with the other two principal axes directed perpendicular to this axis (in the xy-plane, assuming the coordinate system origin to be at the phosphorus atom). Because of the axial symmetry of the tensor, the directions associated with the σ_{11} and σ_{22} components, as pictured in Fig. 9(a), may be interchanged (equivalently, they may be referred to as $\sigma_\perp$, as they both point perpendicular to the C_3 axis).

As expected, the contributions to diamagnetic phosphorus shielding (Table 8) arise primarily from MOs with high phosphorus AO character (see Supporting Information Table S7 for FO contributions to the MOs), with the degree of anisotropy again being dependent upon the degree of s- and p-character of the MO. Nearly all of the diamagnetic shielding (94%) can be accounted for by considering only the MOs in Table 8.

Much the same can be said about the paramagnetic shielding contributions, because out of 112 MOs, only nine must be considered to account for the majority (ca. 63%) of the paramagnetic shielding

Table 6 HF: Significant Paramagnetic Contributions to $\ddot{\sigma}$, Arranged by MO

φ_a	MO	φ_b	MO	σ_{11} (ppm)	σ_{22} (ppm)	σ_{33} (ppm)	σ_{iso} (ppm)	$\langle\varphi_b|R_n|\varphi_a\rangle$
Occupied–Occupied molecular orbital mixing contributions								
3	3σ	4	$1\pi_x$	97.9	0.0	0.0	32.6	$\langle\pi|(R_xR_y)|\sigma\rangle$
3		5	$1\pi_y$	0.0	97.9	0.0	32.6	$\langle\pi|(R_xR_y)|\sigma\rangle$
–	–	–	rem	8.1	8.1	0.0	5.5	–
Occupied–Virtual molecular orbital mixing contributions								
3	3σ	9	$2\pi_x{}^*$	−18.4	0.0	0.0	−6.1	$\langle\pi|(R_xR_y)|\sigma\rangle$
3		10	$2\pi_y{}^*$	0.0	−18.4	0.0	−6.1	$\langle\pi|(R_xR_y)|\sigma\rangle$
4	$1\pi_x$	6	$4\sigma^*$	−56.4	0.0	0.0	−18.8	$\langle\sigma|(R_xR_y)|\pi\rangle$
4		8	$6\sigma^*$	−75.7	0.0	0.0	−25.2	$\langle\sigma|(R_xR_y)|\pi\rangle$
5	$1\pi_y$	6	$4\sigma^*$	0.0	−56.4	0.0	−18.8	$\langle\sigma|(R_xR_y)|\pi\rangle$
5		8	$6\sigma^*$	0.0	−75.7	0.0	−25.2	$\langle\sigma|(R_xR_y)|\pi\rangle$
–	–	–	rem	−55.3	−55.3	0.0	−37.0	–

Table 7   PF₃: Contributions to Phosphorus Chemical Shielding (ppm)[a]

Contribution	σ_{11} (ppm)	σ_{22} (ppm)	σ_{33} (ppm)	σ_{iso} (ppm)	Ω (ppm)	$\Delta\sigma$ (ppm)	κ
σ^d (total)	958.79	958.79	952.98	956.85	–	–	–
σ^p (gauge)	−1.29	−1.29	−1.73	−1.44	–	–	–
σ^p (occ–occ)	−15.34	−15.34	−76.89	−35.86	–	–	–
σ^p (occ–vir)	−871.17	−871.17	−555.41	−765.91	–	–	–
σ^p (total)	−887.80	−887.80	−634.02	−803.20	–	–	–
σ (total)	70.99	70.99	318.96	153.65	247.97	−247.97	1.00
Experiment[b] (10, 146, 147)	–	–	–	222.69	181 ± 5	−181 ± 5	1.00
					228 ± 2	−228 ± 2	1.00
Calculation[c] (148)	–	–	–	235.24	273.95	−273.95	–

[a] TZ2P all-electron basis set on all atoms.
[b] Anisotropic parameters are given for PF₃ dissolved in smectic (top value) and nematic (bottom value) liquid crystal solvents.
[c] Results from high-level calculations.

(Table 9). Occ–occ mixing contributes only slightly to the net paramagnetic shielding tensor, and arises from MO mixing between $e \leftrightarrow e$ and $e \leftrightarrow a_1$ pairs.

The C_{3v} group has the rotational operators $\hat{R}_z$ and $(\hat{R}_x, \hat{R}_y)$, whose IRs are A_2 and E, respectively. By evaluating the selection rule for this point group,
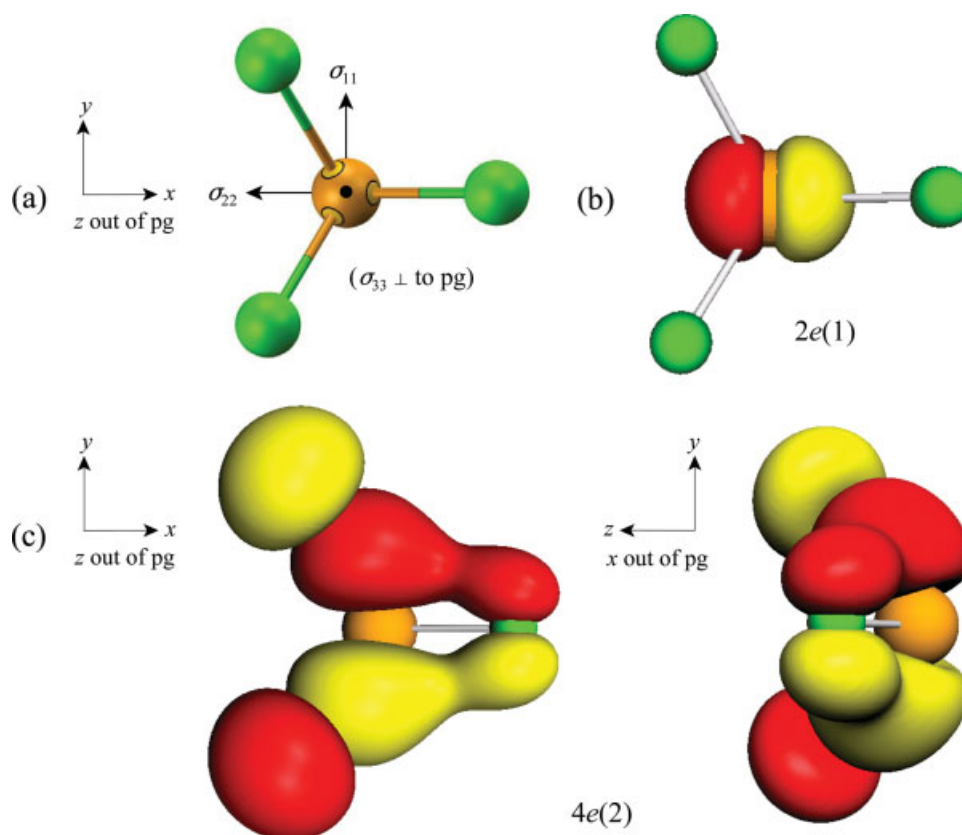

Figure 9   (a) Phosphorus chemical shielding tensor orientation of PF₃ in the molecular frame. ADFview renderings of the (b) 2e(1) and (c) 4e(2) MOs, which do not overlap with one another unless the z rotational operator is applied. To aid in visualization, the 4e(2) MO is provided from two points of view, one along the z-axis (left) and one along the x-axis (right). [Color figure can be viewed in the online issue, which is available at www.interscience.wiley.com.]

Table 8   PF$_3$: Significant Diamagnetic Contributions to $\ddot{\sigma}$, Arranged by MO

φ_p	MO	σ_{11} (ppm)	σ_{22} (ppm)	σ_{33} (ppm)	σ_{iso} (ppm)	Δ_{pc} (ppm)	s char. (%)	p char. (%)
1	$1a_1$	517.1	517.1	517.1	517.1	0.0	100.0	0.0
5	$3a_1$	99.6	99.6	99.6	99.6	0.0	100.0	0.0
6	$2e(1)$	115.1	57.6	115.1	96.0	57.5	0.0	100.0
7	$2e(2)$	57.6	115.1	115.1	96.0	57.5	0.0	100.0
8	$4a_1$	114.5	114.5	57.6	95.5	56.9	0.1	99.9
–	rem	54.9	54.9	48.5	52.7	–	–	–

$$\Gamma(\phi_b) \otimes \Gamma(\hat{R}_n) \otimes \Gamma(\phi_a) = E \otimes \begin{bmatrix} E \\ A_2 \end{bmatrix} \otimes E$$

$$= \begin{bmatrix} 3E + A_2 + A_1 \\ E + A_2 + A_1 \end{bmatrix} \quad (18)$$

it is seen that the contributions to magnetic shielding are nonzero along any of the three coordinate axes, because each element in the rightmost matrix contains the totally symmetric representation for the C_{3v} point group (i.e., A_1). However, calculations reveal that $e \leftrightarrow e$ mixing makes no contribution to the CS tensor for the magnetic field directed along the x and y directions. To understand this, we consider $2e(1) \leftrightarrow 4e(2)$ mixing. If the $2e(1)$ orbital is rotated about the x-axis, it is clear that its orientation does not vary and it remains as pictured in Fig. 9(b). If one then considers the degree of overlap between the $2e(1)$ and $4e(2)$ MOs [Fig. 9(c)], it is seen that there are equal amounts of constructive and destructive orbital overlap, leading to zero net overlap. Rotation of the $2e(1)$ MO about the y-axis leads to the same situa-

tion: there are equal amounts of constructive and destructive MO overlap and therefore there is zero net overlap. It is concluded that this pair of MOs cannot contribute to CS when the magnetic field is along either the x- or y-directions, despite the fact that the integrals cannot be guaranteed to equal zero on the basis of symmetry alone. On the other hand, if the $2e(1)$ MO is rotated about the z-axis, there is significant destructive overlap, corresponding to paramagnetic deshielding contributions. This example demonstrates that it is critical to consider both the selection rule and the degree of overlap of the mixing MOs, and it is shown that this MO pair contributes to deshielding along the z-axis only (along $\boldsymbol{\sigma}_{33}$).

Although $\ddot{\sigma}^d$ is an important factor in determining the overall shielding of a nucleus, it often varies little as one changes the environment about an atom (*vide infra*); hence, $\ddot{\sigma}^p$ is usually more important for comparing changes in the nature of the CS tensor with variation in structure and bonding. In PF$_3$, the occ–vir contributions to $\ddot{\sigma}^p$ dominate the occ–occ contributions by a factor of ca. 20:1. Because of the

Table 9   PF$_3$: Significant Paramagnetic Contributions to $\ddot{\sigma}$, Arranged by MO

φ_a	MO	φ_b	MO	σ_{11} (ppm)	σ_{22} (ppm)	σ_{33} (ppm)	σ_{iso} (ppm)	$\langle \varphi_b | R_n | \varphi_a \rangle$
Occupied–Occupied molecular orbital mixing contributions								
6	$2e(1)$	14	$4e(2)$	0.0	0.0	−49.9	−16.6	$\langle e|R_z|e \rangle$
6		21	$8a_1$	−50.3	0.0	0.0	−16.8	$\langle a_1|(R_x,R_y)|e \rangle$
7	$2e(2)$	13	$4e(1)$	0.0	0.0	−49.9	−16.6	$\langle e|R_z|e \rangle$
7		21	$8a_1$	0.0	−50.3	0.0	−16.8	$\langle a_1|(R_x,R_y)|e \rangle$
8	$4a_1$	13	$4e(1)$	−57.4	0.0	0.0	−19.1	$\langle e|(R_x,R_y)|a_1 \rangle$
8		14	$4e(2)$	0.0	−57.4	0.0	−19.1	$\langle e|(R_x,R_y)|a_1 \rangle$
13	$4e(1)$	21	$8a_1$	66.8	0.0	0.0	22.3	$\langle a_1|(R_x,R_y)|e \rangle$
14	$4e(2)$	21	$8a_1$	0.0	66.8	0.0	22.3	$\langle a_1|(R_x,R_y)|e \rangle$
–	–	–	rem	25.6	25.6	22.9	24.6	–
Occupied–Virtual molecular orbital mixing contributions								
13	$4e(1)$	23	$7e(2)*$	0.0	0.0	−138.9	−46.3	$\langle e|R_z|e \rangle$
13		28	$11a_1*$	−88.8	0.0	0.0	−29.3	$\langle a_1|(R_x,R_y)|e \rangle$
14	$4e(2)$	22	$7e(1)*$	0.0	0.0	−138.9	−46.3	$\langle e|R_z|e \rangle$
14		28	$11a_1*$	0.0	−88.8	0.0	−29.3	$\langle a_1|(R_x,R_y)|e \rangle$
21	$8a_1$	22	$7e(1)*$	−493.2	0.0	0.0	−164.4	$\langle e|(R_x,R_y)|a_1 \rangle$
21		23	$7e(2)*$	0.0	−493.2	0.0	−164.4	$\langle e|(R_x,R_y)|a_1 \rangle$
–	–	–	rem	−290.0	−290.0	−277.6	−285.9	–

$$7e(1) \otimes (\hat{R}_x, \hat{R}_y) \otimes 8a_1 = E \otimes E \otimes A_1 \supseteq A_1$$
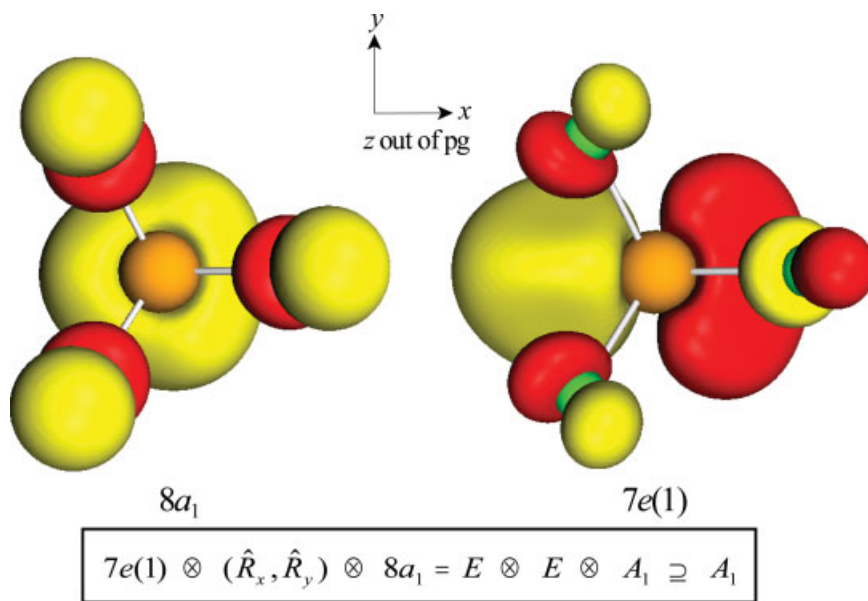
Figure 10   The most significant contribution to the paramagnetic shielding tensor along the σ_{11} direction is due to $8a_1 \leftrightarrow 7e(1)$. As outlined in the box, the doubly degenerate rotational operator possesses the correct symmetry for mixing these two MOs. If the $8a_1$ MO is rotated about the y-axis, there is clearly destructive overlap with the $7e(1)$ MO, and as σ_{11} and the y-axis are parallel, this pair should produce shielding along σ_{11}, in agreement with the calculated direction. [Color figure can be viewed in the online issue, which is available at www.interscience.wiley.com.]

pronounced anisotropic fashion in which pairwise MO mixing contributes to $\ddot{\sigma}^p$, the observed isotropic shielding value, as well as the magnitude of the shielding anisotropy, can be rationalized by considering the occ–vir contributions to $\ddot{\sigma}^p$. As mentioned earlier, the six pairs of MOs listed in Table 9 account for approximately 63% of all occ–vir contributions to the isotropic shielding value. Within this set, it is clear that $8a_1$ (HOMO) $\leftrightarrow 7e^*$ (LUMO) mixing contributes very significantly along the σ_{11} and σ_{22} directions (the $8a_1 \leftrightarrow 7e(1)^*$ contribution to σ_{11} along the y axis is illustrated in Fig. 10), with other MO pairs making less significant contributions along σ_{33}. Therefore, it is primarily this MO pair which leads to the pronounced shielding anisotropy observed in the ^{31}P NMR spectra of PF$_3$, in agreement with earlier findings (*150*). The contribution that this MO pair makes is expected to be quite substantial, as $7e^*$ has very high phosphorus character (92.1% of this MO is from either the $3p_x$ or $3p_y$ AOs of the phosphorus, Supporting Information Table S7). In addition, HOMO/LUMO mixing necessarily means that ΔE is at its minimum value (for occ–vir mixing). This can be contrasted with the shielding produced due to $4e \leftrightarrow 11a_1^*$. This pair contributes in a

more modest fashion to $\ddot{\sigma}^p$ due to the decreased phosphorus character of the occupied orbital, as well as a significantly larger ΔE (16.74 eV, when compared with 6.55 eV for $8a_1 \leftrightarrow 7e^*$). A partial MO diagram for PF$_3$, highlighting the MOs which contribute substantially to $\ddot{\sigma}^p$, as well renderings of many of the MOs with major paramagnetic shielding contributions, are provided in Fig. 11.

Water, H$_2$O

Unlike the previous three examples, the paramagnetic oxygen CS tensor in water is influenced by a number of MO pairs (*vide infra*). In addition, the oxygen shielding tensor has not been experimentally measured by ssNMR, likely due to the substantial [17]O quadrupolar interaction which would dominate the solid-state ^{17}O NMR spectrum (*151, 152*). Despite not having this experimental data, H$_2$O is an important system to investigate, because the oxygen CS parameters can be drastically affected by hydrogen bonding interactions.

Isotropic Oxygen CS.   The isotropic CS value at the oxygen nucleus in a geometry-optimized water
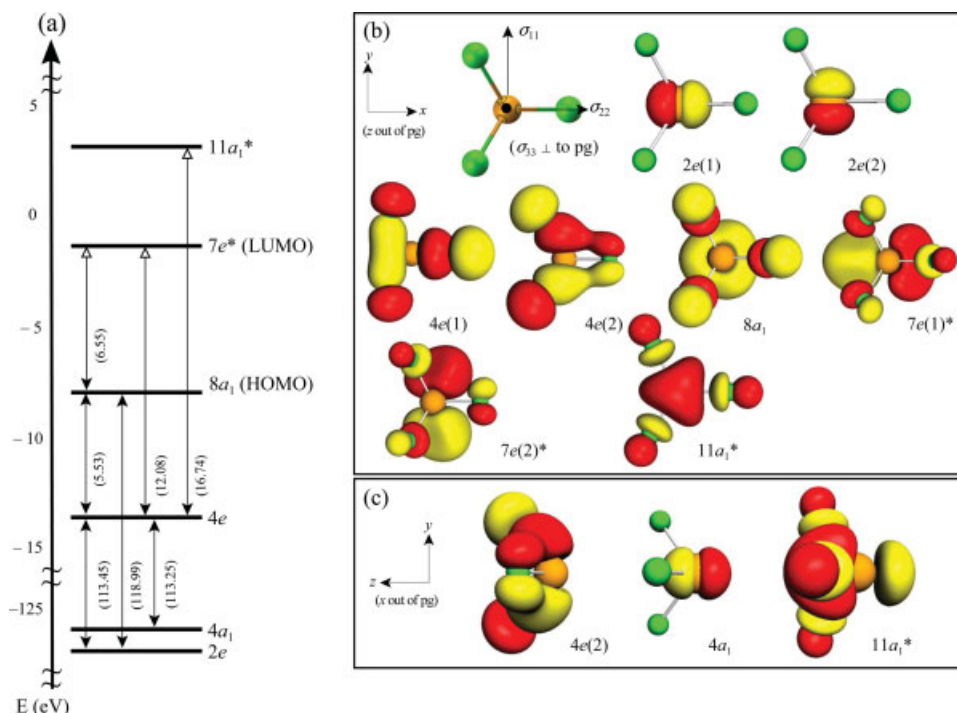
Figure 11   (a) Partial MO diagram for PF_3, showing MOs that make significant contributions to the paramagnetic shielding tensor. (b) Renderings of these key MOs are provided, as viewed along the z (b) and x (c) directions. [Color figure can be viewed in the online issue, which is available at www.interscience.wiley.com.]

molecule, $\sigma_{iso}(^{17}O)$, is calculated to be 322.75 ppm (Table 10; see Supporting Information Table S1 for the optimized geometry), in very good agreement with previously reported hybrid computational-experimental (*155*, *156*) and high-level *ab initio* (*157*) values. The diamagnetic and paramagnetic portions of isotropic oxygen CS are calculated to be 384.65 ppm and –61.90 ppm, respectively. Oxygen CS calculations were also carried out upon CO and H_2CO (Table 10). It is observed that though σ_{iso}^d varies only slightly ($\Delta\sigma_{iso}^d$ is ca. 15 ppm for the set of three molecules), the total magnetic shielding at the nucleus can change by very significant amounts. In fact, $\sigma_{iso}(^{17}O, H_2CO)$ is nearly 800 ppm less than in H_2O. It is abundantly clear that paramagnetic deshielding is the source of this variation: while it is very modest in H_2O, it is clearly the dominant feature in the total oxygen shielding in CO and H_2CO. Relative to $\ddot\sigma^p$ of H_2O, the most notable changes in $\ddot\sigma^p$ of CO and H_2CO are from the occ–vir contributions, whereas the changes in occ–occ are less pronounced, but still significant.

Anisotropic Oxygen CS.   The span of the oxygen shielding tensor (Table 11) is calculated to be 59.07

ppm, with both diamagnetic and paramagnetic shielding mechanisms making significant contributions. The skew ($\kappa(^{17}O) = 0.16$) indicates that all of the principal components are distinct and that the solid-state powder pattern (neglecting quadrupolar broadening) is distributed approximately centrosymmetrically about σ_{iso}. A water molecule has C_{2v} symmetry (see Supporting Information Table S8 for character table). The calculated orientation [Fig. 12(a)] of the oxygen shielding tensor is again constrained by molecular symmetry: $\boldsymbol\sigma_{11}$ points perpendicular to the molecular plane and lies parallel to the x-axis (in the xz-mirror plane), $\boldsymbol\sigma_{22}$ lies along the C_2 axis and $\boldsymbol\sigma_{33}$ is directed parallel to the y-axis (in the yz-mirror plane).

Total diamagnetic shielding is again observed to be heavily dependent upon core MOs that possess high oxygen character (Table 12), with the most significant offering (270.6 ppm) provided by the $1a_1$ MO, which is essentially the $1s$ AO on the oxygen (Supporting Information Table S9). The four MOs listed in Table 12 account for 98% of the total diamagnetic shielding. The degree of anisotropy of each contribution again appears to increase with decreasing MO s-character.

Table 10   H$_2$O, CO, and H$_2$CO: Contributions to Isotropic Oxygen Chemical Shielding (ppm)[a]

Contribution	H$_2$O (*156, 157*)	CO (*156, 157*)	H$_2$CO (*140, 153, 154*)
σ^d	384.65	400.69	399.56
σ^p (gauge)	−0.66	0.00	−1.41
σ^p (occ–occ)	160.28	−16.94	−13.15
σ^p (occ–vir)	−221.50	−459.85	−833.75
σ^p (total)	−61.90	−476.79	−848.30
σ_{iso} (total)	322.75	−76.10	−448.74
Experiment	323.6 ± 0.6	−62.74 ± 0.59	−427.1 ± 100
Calculation[b]	324.0 ± 1.5	−62.3 ± 1.5	−383.1

[a] TZ2P all-electron basis set on all atoms.
[b] Results from high-level calculations.

The total oxygen paramagnetic shielding tensor has a few very important contributors (Table 13). Nearly all (95%) of the $\ddot{\sigma}^p$(occ–occ) contributions are accounted for by three MO pairs, with each pair making shielding contributions along a unique direction. The $1b_2 \leftrightarrow 3a_1$ and $1b_2 \leftrightarrow 1b_1$ pairs [Figs. 12(b,c)] make the most pronounced contributions to $\ddot{\sigma}^p$. Using group theory, it is shown below that $1b_2 \leftrightarrow 3a_1$ must produce shielding along σ_{11}, while $1b_2 \leftrightarrow 1b_1$ leads to shielding along σ_{22}. The C_{2v} point group has rotational operators of B_2, B_1, and A_2 symmetry for rotations about the x-, y-, and z-axes, respectively. The direct products are evaluated in the usual manner (first for $1b_2 \leftrightarrow 3a_1$, followed by $1b_2 \leftrightarrow 1b_1$):

$$\Gamma(\phi_b)\otimes\Gamma(\hat{R}_n)\otimes\Gamma(\phi_a)=A_1\otimes\begin{bmatrix}B_2\\B_1\\A_2\end{bmatrix}\otimes B_2=\begin{bmatrix}A_1\\A_2\\B_1\end{bmatrix} \quad (19)$$

$$\Gamma(\phi_b)\otimes\Gamma(\hat{R}_n)\otimes\Gamma(\phi_a)=B_1\otimes\begin{bmatrix}B_2\\B_1\\A_2\end{bmatrix}\otimes B_2=\begin{bmatrix}B_1\\B_2\\A_1\end{bmatrix}. \quad (20)$$

Elements in the rightmost matrices in [**19**] and [**20**] contain the totally symmetric representation, A_1 only when the $\hat{R}_x$ and $\hat{R}_z$ operators are used. Because σ_{11} is along x and σ_{22} is along z [Fig. 12(a)], $1b_2 \leftrightarrow 3a_1$ may only produce shielding along σ_{11} and $1b_2 \leftrightarrow 1b_1$ can contribute to CS only along σ_{22}. In addition to being allowed by symmetry, it is expected that these MO pairs will produce large occ–occ paramagnetic shielding contributions, because of relatively small ΔE values (only 5.83 eV separates $1b_1$ from $1b_2$) coupled with high oxygen MO character(s) and the presence of a substantial amount of nonbonding electron density. The small separation in energies between the $1b_2$, $3a_1$, and $1b_1$ MOs is likely the reason the total $\ddot{\sigma}^p$(occ–occ) contributions are similar in magnitude to the occ–vir MO mixing contributions, in contrast to ethene and PF$_3$. The HOMO-LUMO energy gap ($\Delta E = 6.32$ eV) is larger than the energy separations between the three important occupied orbitals (Fig. 13). The most pronounced occ–vir contributions to $\ddot{\sigma}^p$ (i.e., $1b_2 \leftrightarrow 2b_1^*$, $1b_1 \leftrightarrow 3b_2^*$) arise from MOs with moderate-to-high oxygen p-character in both the occupied and virtual MOs. Smaller contri-

Table 11   H$_2$O: Contributions to Oxygen Chemical Shielding (ppm)[a]

Contribution	σ_{11} (ppm)	σ_{22} (ppm)	σ_{33} (ppm)	σ_{iso} (ppm)	Ω (ppm)	$\Delta\sigma$ (ppm)	κ
σ^d (total)	370.61	379.47	403.88	384.65	–	–	–
σ^p (gauge)	−1.97	0.00	0.00	−0.66	–	–	–
σ^p (occ–occ)	226.80	204.52	49.51	160.28	–	–	–
σ^p (occ–vir)	−300.68	−264.32	−99.57	−221.50	–	–	–
σ^p (total)	−75.85	−59.80	−50.05	−61.90	–	–	–
σ (total)	294.76	319.67	353.83	322.75	59.07	−46.62	0.16
Experiment (*156*)	–	–	–	323.6	–	–	–
Calculation[b] (*157*)	–	–	–	324.00	–	–	–

[a] TZ2P all-electron basis set on all atoms.
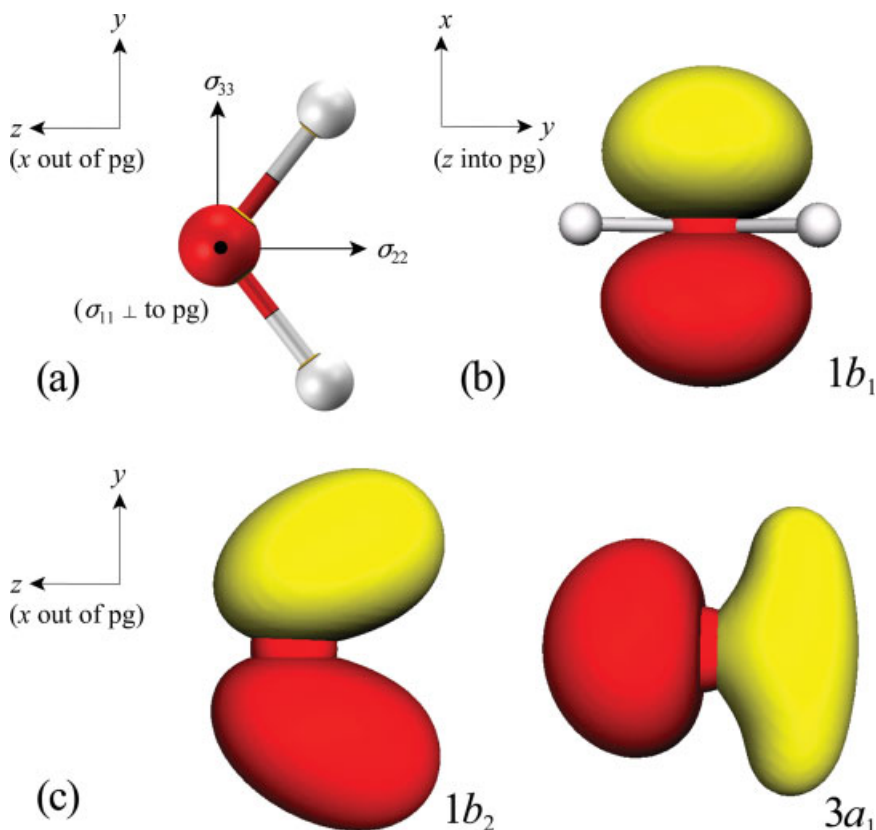[b] Results from high-level calculations.

Figure 12 (a) Oxygen chemical shielding tensor of water in the frame of the molecule. (b, c) ADFview renderings of MOs which make significant contributions to chemical shielding: the $1b_2 \leftrightarrow 3a_1$ and $1b_2 \leftrightarrow 1b_1$ MO pairs contribute significantly to the paramagnetic shielding tensor along the σ_{11} and σ_{22} shielding directions, respectively. [Color figure can be viewed in the online issue, which is available at www.interscience.wiley.com.]

butions to occ–vir shielding are provided by the same occupied MOs, but the mixing occurs with virtual MOs that are high in H s-character (e.g., the $4a_1$* and $5a_1$* MOs).

Selected Literature Examples Revisited

As discussed in the theoretical background section, a number of literature examples exist which possess some of the elements of the CS discussions presented here. MO-by-MO analysis and/or the concept of wave functions/MOs being subjected to angular momentum operators are usually presented. When discussing contributions to CS, the aspect of group theory is rarely mentioned (*46*, *158*), and no case can be found where the direct products of the symmetry representations of the MOs and rotational operators are evaluated. As the fundamental basis for describing CS remains largely unchanged (i.e., Ramsey's equations), it is instructive to revisit a few of the similar accounts in the literature, to apply (briefly) the group theory aspect of the treatment.

Table 12   H$_2$O: Significant Diamagnetic Contributions to $\ddot{\sigma}$, Arranged by MO

φ_p	MO	σ_{11} (ppm)	σ_{22} (ppm)	σ_{33} (ppm)	σ_{iso} (ppm)	Δ_{pc} (ppm)	s char. (%)	p char. (%)
1	$1a_1$	270.6	270.6	270.6	270.6	0.0	100.0	0.0
2	$2a_1$	39.5	39.3	37.4	38.7	2.1	93.0	7.0
4	$3a_1$	35.1	23.3	34.3	30.9	11.8	85.0	14.0
5	$1b_1$	22.3	44.9	44.3	37.2	22.6	1.0	99.0
–	rem	3.1	1.4	17.3	7.3	–	–	–

Table 13 H_2O: Significant Paramagnetic Contributions to $\ddot{\sigma}$, Arranged by MO

φ_a	MO	φ_b	MO	σ_{11} (ppm)	σ_{22} (ppm)	σ_{33} (ppm)	σ_{iso} (ppm)	$\langle\varphi_b|R_n|\varphi_a\rangle$
Occupied–Occupied molecular orbital mixing contributions								
3	$1b_2$	4	$3a_1$	209.4	0.0	0.0	69.8	$\langle a_1|R_x|b_2\rangle$
3		5	$1b_1$	0.0	204.5	0.0	68.2	$\langle b_1|R_z|b_2\rangle$
4	$3a_1$	5	$1b_1$	0.0	0.0	42.4	14.1	$\langle b_1|R_y|a_1\rangle$
–	–	–	rem	17.4	0.0	7.1	8.2	–
Occupied–Virtual molecular orbital mixing contributions								
3	$1b_2$	6	$4a_1{}^*$	−31.6	0.0	0.0	−10.5	$\langle a_1|R_x|b_2\rangle$
3		8	$5a_1{}^*$	−35.7	0.0	0.0	−11.9	$\langle a_1|R_x|b_2\rangle$
3		10	$6a_1{}^*$	−74.7	0.0	0.0	−24.9	$\langle a_1|R_x|b_2\rangle$
3		11	$2b_1{}^*$	0.0	−108.9	0.0	−36.3	$\langle b_1|R_z|b_2\rangle$
4	$3a_1$	9	$3b_2{}^*$	−68.0	0.0	0.0	−22.7	$\langle b_2|R_x|a_1\rangle$
5	$1b_1$	6	$4a_1{}^*$	0.0	0.0	−31.7	−10.6	$\langle a_1|R_y|b_1\rangle$
5		8	$5a_1{}^*$	0.0	0.0	−50.3	−16.8	$\langle a_1|R_y|b_1\rangle$
5		9	$3b_2{}^*$	0.0	−98.4	0.0	−32.8	$\langle b_2|R_z|b_1\rangle$
–	–	–	rem	−90.7	−57.0	−17.6	−55.0	–

Acetylene (Ethyne), C_2H_2.   The anisotropic carbon CS of acetylene has been discussed in detail from a theoretical standpoint on at least two other occasions (*38*, *41*), motivated by the experimental observations of Grant and co-workers (*102*). Acetylene has $D_{\infty h}$ symmetry, which possesses three rotational operators: a doubly degenerate set, $(\hat{R}_x, \hat{R}_y)$, which can be

associated with the Π_g IR, and the $\hat{R}_z$ operator, which belongs to the Σ_g^- IR. The experimentally measured carbon CS tensor in acetylene is axially symmetric ($\kappa(^{13}C) = +1.00$) with a substantial span of 240 ppm. Because the symmetry of the molecule can be represented using a linear point group, there is no paramagnetic shielding along the z-axis of the mole-
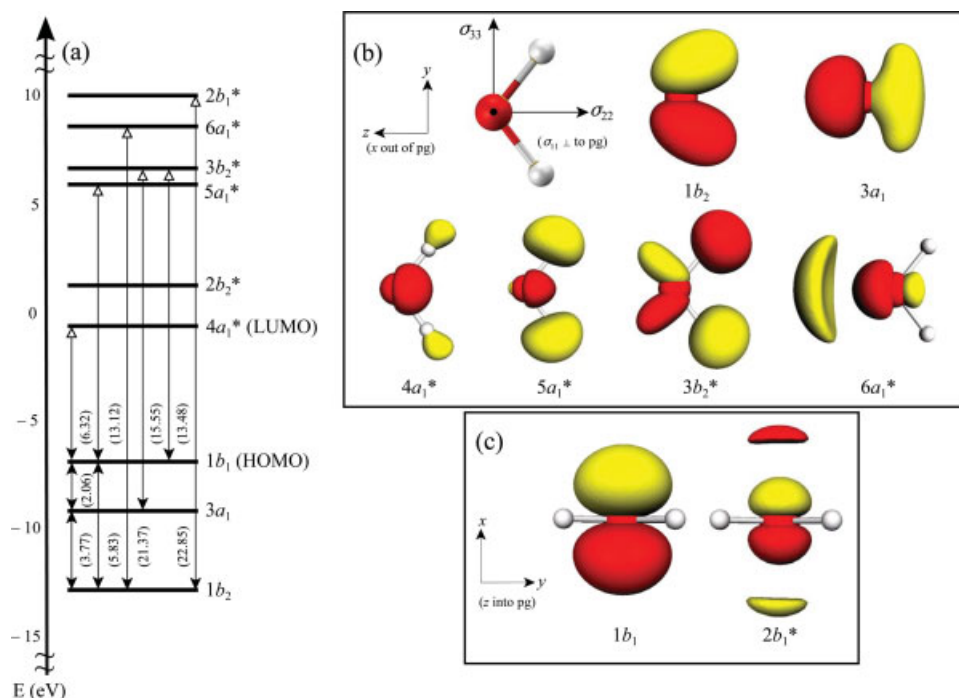

Figure 13   (a) Partial MO diagram for water, highlighting MOs that make significant contributions to the paramagnetic shielding tensor. (b) Visual representations of the important MOs, generated using the ADFview software, along the (b) *x* and (c) *z* directions. [Color figure can be viewed in the online issue, which is available at www.interscience.wiley.com.]
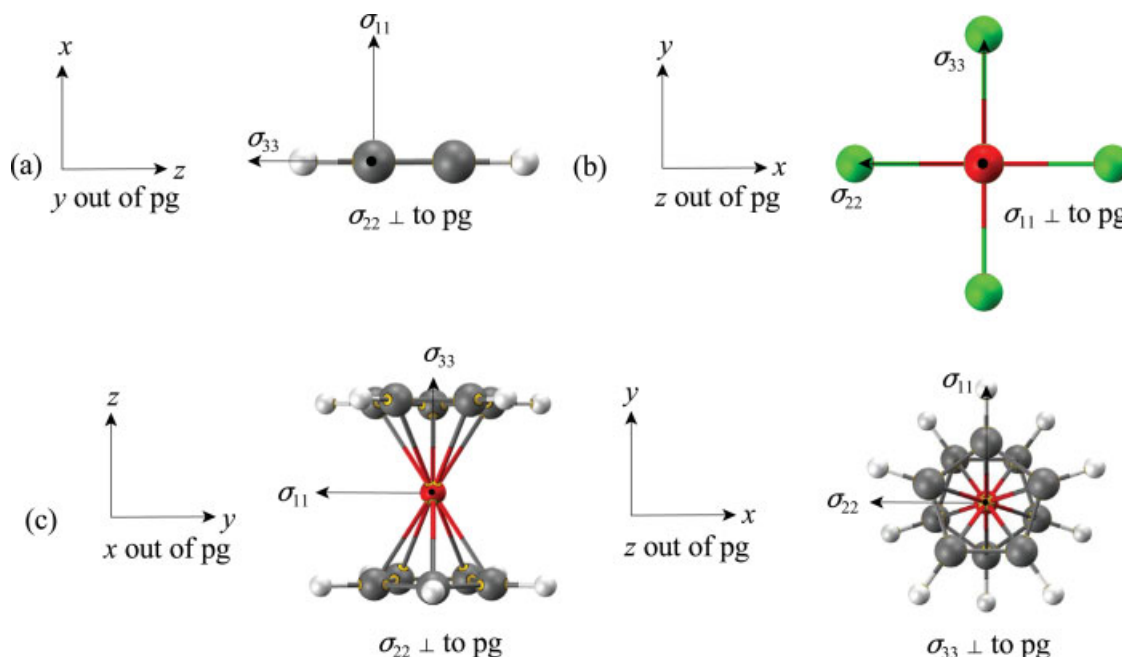
Figure 14 Various chemical shielding tensor orientations in appropriate molecular frames. (a) The carbon CS tensor orientation of acetylene. (b) The platinum CS tensor orientation of $PtCl_4^{2-}$. (c) The aluminum CS tensor orientation of $[Cp_2Al]^+$ (the molecule used in computations by Schurko et al.; the tensor orientation is thought to be equivalent in $[Cp^*_2Al]^+$) (121), as viewed perpendicular (left) and parallel (right) to the C_5 axis of the molecule. [Color figure can be viewed in the online issue, which is available at www.interscience.wiley.com.]

cule [Fig. 14(a)]. It was previously reported that the experimental spectrum can be rationalized by considering the mixing between an occupied σ_g MO, whose symmetry representation in $D_{\infty h}$ is Σ_g^+, and two virtual π_g MOs, which may be represented as Π_g. The direct product of the symmetry representations of these important shielding MOs with the rotational operators is:

$$\Gamma(\phi_b) \otimes \Gamma(\hat{R}_n) \otimes \Gamma(\phi_a) = \Pi_g \otimes \begin{bmatrix} \Pi_g \\ \Sigma_g^- \end{bmatrix} \otimes \Sigma_g^+$$

$$= \begin{bmatrix} \Sigma_g^+ + \Sigma_g^- + \Delta_g \\ \Pi_g \end{bmatrix}. \quad (21)$$

As Σ_g^+ is the totally symmetric representation of this point group, constructive overlap of this sort is allowed by symmetry only when the degenerate $(\hat{L}_x, \hat{L}_y)$ operators are applied. Thus, paramagnetic shielding contributions are allowed only along the x- and y-directions, in agreement with the calculated directions of Wiberg et al. (explicit discussions in this account pertained to σ_{xx} shielding; σ_{yy} was assumed based upon symmetry arguments) (41). By observing the fashion in which the σ_g and π_g MOs transform under the $\hat{L}_x$ operator, it was established in

the previous accounts that $\sigma_g \leftrightarrow \pi_g$ will lead to positive overlap with one another and hence contribute to shielding. Because of the symmetry of the doubly degenerate π_g orbitals, the magnitude of paramagnetic deshielding will be equal along the x and y directions. As $\sigma_g \leftrightarrow \pi_g$ is the dominant MO pair, the resultant shielding tensor is axially symmetric, in accordance with the experimental findings. The actual value of the span is determined by the degree of overlap between the mixing MO pairs, in addition to ΔE, but it is worth noting that the two pairs of MOs mentioned in this section account for about 95% of the calculated span (41).

PtX_4^{2-} Series. In a recent publication by Ziegler et al., the zeroth-order relativistic approximation (ZORA) DFT method was shown to be quite accurate in the calculation of ^{195}Pt NMR CS tensors for a series of *cis-* and *trans-*PtX_2L_2 (X = halogen; L = NH_3, PMe_3, SMe_2, or $AsMe_3$) complexes (i.e., within 2–3% of the total platinum CS range) (118). Theoretical platinum CS calculations were also carried out upon PtX_4^{2-} dianions (discussions pertaining to the importance of unspecific solvent effects (159) and shielding contributions within the natural localized

MO/natural bond orbital model (119) have also recently appeared in the literature for PtCl$_4^{2-}$) and it was noted that two MO pairs, leading to platinum CS along z, are responsible for approximately 40% of the calculated paramagnetic shielding in the series where X = Cl, Br, I. Both of these involved $d_{xy} \leftrightarrow d_{x^2-y^2}$ type mixing (a pure d-orbital model for the platinum valence was used in their discussion). Each of the complexes may be represented using the D_{4h} point group [Fig. 14(b)] for the shielding tensor orientation), hence, $\Gamma(d_{xy}) = B_{2g}$ and $\Gamma(d_{x^2-y^2}) = B_{1g}$. Available rotational operators and their representations (in brackets) are $(\hat{R}_x, \hat{R}_y)$, (E_g) and $\hat{R}_z$ (A_{2g}). The direct product is evaluated as:

$$\Gamma(\phi_b) \otimes \Gamma(\hat{R}_n) \otimes \Gamma(\phi_a) = B_{1g} \otimes \begin{bmatrix} E_g \\ A_{2g} \end{bmatrix} \otimes B_{2g}$$

$$= \begin{bmatrix} 2E_g \\ A_{1g} \end{bmatrix}. \quad (22)$$

The totally symmetric representation in D_{4h} is A_{1g}, hence only $\hat{L}_z$ may produce magnetic shielding via $d_{xy} \leftrightarrow d_{x^2-y^2}$, in agreement with the calculated direction in the earlier report. The two $d_{xy} \leftrightarrow d_{x^2-y^2}$ MO pairs are calculated to contribute 10,000 ppm to $\ddot{\sigma}^p$ along the z-direction in PtCl$_4^{2-}$ (slightly less for the other two complexes in this series), constraining σ_{11} to point perpendicular to the molecular plane. Because of the symmetry of the molecule, the calculated shielding tensor is axially symmetric, but this is the first case discussed in this article where $\kappa = -1.0$. This value is due, in large part, to the pronounced uniaxial deshielding resulting from the overlap of the two MO pairs discussed earlier. Other conclusions made in this previous report mirror ours: i) a greater ΔE between mixing MO pairs typically leads to decreased contributions to $\ddot{\sigma}(^{195}\text{Pt})$ and ii) orbital overlap must be considered to explain the magnitudes of contributions to $\ddot{\sigma}^p$ when ΔE values are very similar. Along the series from X = Cl, Br, and I, it was established that σ_{iso}^p sequentially decreased, and that ΔE values decreased very slightly (less than 1 eV) (118). Because of the dominant contributions from $d_{xy} \leftrightarrow d_{x^2-y^2}$ type MO mixing, the decreased σ_{iso}^p was attributed almost entirely to the decreasing platinum character of the MOs.

The Decamethylaluminocenium Cation, [Cp$_2^*$Al]$^+$. The aluminum shielding anisotropy for [Cp$_2^*$Al]$^+$ was found to be substantial and nearly axially symmetric (121), with $\Omega(^{27}\text{Al}) = 108.1$ ppm and $\kappa(^{27}\text{Al}) = +0.88$ [Fig. 14(c)]. For this study, the molecular symmetry chosen by the authors was D_{5d}, which is

slightly lower in energy than the D_{5h} form. Because of the presence of axial molecular symmetry, the observed skew of approximately +1.00 is unsurprising. The pronounced span can be attributed to a number of mixing MO pairs (i.e., there is no dominant MO pair; however, the magnitude which each significant MO pair contributes is roughly the same), although it appears that the prominent $\ddot{\sigma}^p$(occ–occ) contributions are all due to the $2e_{1u}$ MO mixing with a virtual a_{2u} MO. In each case, a contribution is made to $\sigma_\perp$ (along σ_{11} or σ_{22}). Available rotation operators (symmetry representations in brackets) are $(\hat{R}_x, \hat{R}_y)$ (E_{1g}) and $\hat{R}_z$ (A_{2g}). Evaluation of the appropriate direct product proceeds as follows:

$$\Gamma(\phi_b) \otimes \Gamma(\hat{R}_n) \otimes \Gamma(\phi_a) = A_{2u} \otimes \begin{bmatrix} E_{1g} \\ A_{2g} \end{bmatrix} \otimes E_{1u}$$

$$= \begin{bmatrix} A_{1g} + A_{2g} + E_{2g} \\ E_{1g} \end{bmatrix}. \quad (23)$$

Mixing of MO pairs of these symmetries with the $\hat{L}_z$ operator is forbidden; hence, no shielding can be produced along the C_5 axis of the molecule (i.e., the z-direction or $\sigma_\parallel/\sigma_{33}$). Mixing of these types of MOs is only symmetry-allowed in a direction perpendicular to the axis of rotation (i.e., the xy-plane or $\sigma_\perp$). The magnitude that each $e_{1u} \leftrightarrow a_{2u}$ pair contributes to $\ddot{\sigma}^p$(occ–vir) is moderate, because of sizeable ΔE values, of which in this series of MOs, the smallest value is 71.76 eV (i.e., 6.92 MJ mol^{-1}). In this previous report, it was found that only $e_{1u} \leftrightarrow e_{1u}$ type MO mixing leads to shielding along $\sigma_\parallel$ (σ_{33}). Because of the presence of more available a_{2u} MOs, (5 are deemed significant) relative to e_{1u} MOs (two are found to be important to $\ddot{\sigma}^p$), it must be concluded that $e_{1u} \leftrightarrow a_{2u}$ type deshielding must contribute more to $\ddot{\sigma}^p$ than $e_{1u} \leftrightarrow e_{1u}$. Therefore, the aluminum shielding tensor must be oriented as in Fig. 14(c), in agreement with the *ab initio* calculations included in the literature account.

CONCLUSIONS

Herein, we have presented an elementary introduction for discussing the origins of CS, and demonstrated that experimentally observed and theoretically calculated CS tensor parameters are intimately related to molecular symmetry. If symmetry elements are present in a molecule, they play a crucial role in determining the orientation of the principal components of the shielding tensor. Direct

products involving the IRs of MOs and rotational operators, and simple visualization of MO mixing using charge rotation, can be used to qualitatively explain CS tensor orientations, and more importantly, changes in CS parameters with alterations of chemical environments.

In most cases, diamagnetic shielding does not vary in a pronounced fashion as one changes the chemical environment about a particular nucleus, as the core AOs of an atom are typically the largest determinants of diamagnetic shielding character. Variation in CS arising from differences/changes in chemical bonding can usually be attributed to changes in paramagnetic shielding, which may be understood via the mixing of MOs using the direct product model presented herein. If the totally symmetric representation of a point group is contained in reduction of the direct product, then MO mixing is allowed by symmetry. The direction of symmetry-allowed (de)shielding is always generated by the rotational operator, such that $\hat{L}_n$ will lead to a (de)shielding contribution parallel to the n-axis. Although qualitative models are adequate for examining MO pair symmetries and CS tensor axes, the magnitudes of the various CS tensor contributions are best determined using computational techniques and analyses of MO contributions like those available in the ADF suite. The most important factors determining the magnitude of CS contributions are the energy separation (ΔE) between the mixing MOs, the atomic characters of the mixing MOs, and the degree of MO mixing induced by the angular momentum operators.

ACKNOWLEDGMENTS

APPENDIX A

Derivation of the First-Order (Secular) Shielding Response

To display the chemical shielding (CS) tensor, Hansen and Bouman (78) proposed the concept of a shielding response vector, (**T**), which is defined as the shielding field per unit of **B**$_0$:

$$\mathbf{T} = \ddot{\sigma} \cdot \hat{u}_{\mathbf{B_0}} \tag{A1}$$

where $\hat{u}_{\mathbf{B_0}}$ is a unit vector along **B**$_0$. The shielding response vector is decomposed into spherical coordinates (Fig. A1) in the frame of the molecule,

$$\mathbf{T} = T_{\mathbf{B_0}}(\theta, \phi)\hat{u}_{\mathbf{B_0}} + T_\theta(\theta, \phi)\hat{u}_\theta + T_\phi(\theta, \phi)\hat{u}_\phi \tag{A2}$$

where the usual Cartesian-to-spherical coordinate transformations are present ($x = T \cos\varphi\sin\theta$, $y = T \sin\varphi\sin\theta$ and $z = T\cos\theta$) and hence **T** and $\hat{u}_{\mathbf{B_0}}$ as column vectors are:

$$\mathbf{T} = \begin{bmatrix} T \cos\phi \sin\theta \\ T \sin\phi \sin\theta \\ T \cos\theta \end{bmatrix}, \quad \hat{u}_{\mathbf{B_0}} = \begin{bmatrix} \cos\phi \sin\theta \\ \sin\phi \sin\theta \\ \cos\theta \end{bmatrix}. \tag{A3}$$
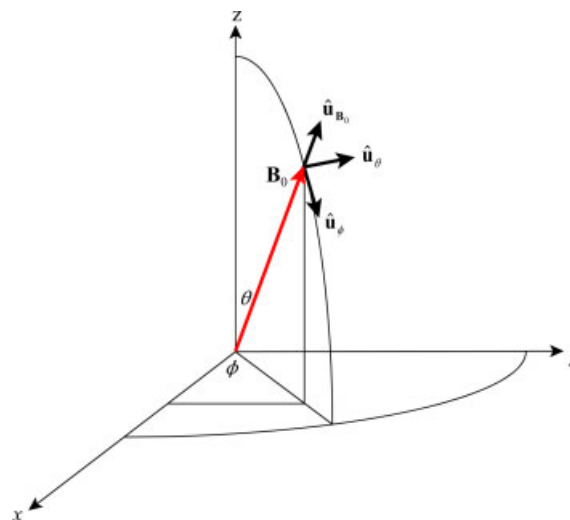

Figure A1 Spherical coordinate system and first-order shielding response unit vectors, as defined in the Appendix. [Color figure can be viewed in the online issue, which is available at www.interscience.wiley.com.]

Using [A3], [3] and the knowledge that the first-order response is symmetric ($\sigma_{ij} = \sigma_{ji}$), the response value along the applied field is calculated:

$$T_{\mathbf{B_0}}(\theta, \phi) \equiv \hat{u}^*_{\mathbf{B_0}} \cdot \ddot{\sigma} \cdot \hat{u}_{\mathbf{B_0}} \equiv T_{\|}(\theta, \phi)$$
$$= \sin^2 \theta [\sigma_{xx} \cos^2 \phi + \sigma_{yy} \sin^2 \phi + \sigma_{xy} \sin 2\phi]$$
$$+ \sin 2\phi [\sigma_{xz} \cos \phi + \sigma_{yz} \sin \phi] + \cos^2 \theta \; \sigma_{zz} \qquad (A4)$$

The remaining response values, which belong to the perpendicular shielding response, may be derived in a similar fashion, although we will omit the derivation here as these response values cannot currently be reliably measured.

APPENDIX B

Calculating CS Using the ADF/GIAO/DFT Methodology

Although Ramsey's formalism, as described earlier, is quite instructive when rationalizing CS in molecules, different models are implemented by computational software for the calculation of $\ddot{\sigma}$. The ADF suite of programs (108, 127, 160) uses Slater-type orbital (STO) functions to describe the basis set elements (i.e., the AOs) which constitute the single-electron wave functions. They are of the form $\phi(r) = \Upsilon_{lm_l}(\Omega) r^l e^{-\alpha r}$, with $\Upsilon_{lm_l}(\Omega)$ describing the angular shape of the element and the remainder pertaining to radial character. The GIAO formalism, widely regarded to be at least marginally superior to other gauge-including methods (161), places individual gauges at the centre of each AO, resulting in a magnetic-field dependent basis, $\phi(\mathbf{r}) \rightarrow \phi_\mu(\mathbf{r}, \mathbf{B_0})$, where the μ identifies that a gauge has been placed at the centre of the AO. The gauge is introduced through a complex exponential function, such that:

$$\phi_\mu(\mathbf{r}, \mathbf{B_0}) = \exp\left[-\frac{i}{2}(\mathbf{B_0} \frown \mathbf{r}_N) \cdot \mathbf{r}_k\right] \phi(\mathbf{r}) \qquad (A5)$$

where $\mathbf{r}_N$ and $\mathbf{r}_k$ are the position vectors of the nucleus and electron, respectively, and [A5] is in atomic units.

DFT according to the formalism of Kohn and Sham (109) (KS) proposes the following exact expression for the ground-state electronic energy of a system (35, 162):

$$E_0 = -\frac{1}{2}\sum_k \langle \psi_k | \nabla^2 | \psi_k \rangle - \int V(\mathbf{r})\rho(\mathbf{r}) d\mathbf{r}$$
$$+ \frac{1}{2} \iint \frac{\rho(\mathbf{r})\rho(\mathbf{r}')}{|\mathbf{r} - \mathbf{r}'|} d\mathbf{r} d\mathbf{r}' + E_{xc}[\rho] \qquad (A6)$$

where ψ_k is the spatial portion of a one-electron wave function which represents the kth orbital, $V(\mathbf{r})$ is an external (nuclear) potential function, $\rho(\mathbf{r})$ is the total electron density of the system and E_{XC} is a functional that describes electron exchange and correlation effects. If E_{XC} is known exactly, [A6] would be exact and according to KS, all ground- and excited-state electronic properties could be determined precisely. Unfortunately, E_{XC} is not exactly known, although much effort has gone into developing suitable representations (162–172).

Field-free one-electron wave functions, $\Phi_q(\mathbf{r}, \mathbf{B_0})$, may be built up using GIAOs:

$$\Phi_q(\mathbf{r}, \mathbf{B_0}) = \sum_\mu c_{\mu q} \; \phi_\mu(\mathbf{r}, \mathbf{B_0}) \qquad (A7)$$

where $c_{\mu q}$ is the field-free expansion coefficient. These are subsequently expanded into wave functions which account for the magnetic field, $\psi_p(\mathbf{r}, \mathbf{B_0})$, using the method of Pople et al. (173):

$$\psi_p(\mathbf{r}, \mathbf{B_0}) = \sum_q u_{qp} \Phi_q(\mathbf{r}, \mathbf{B_0}) \qquad (A8)$$

where u_{qp} is the field-including expansion coefficient, which carries within it an inverse ΔE dependence (51). The MOs built up using [A7–A8] from the GIAOs in [A5] can then be used to calculate $\ddot{\sigma}$. CS tensor components (σ_{ij}) may be defined alternatively, but equivalently as in [4], as the second derivative of the electronic energy with respect to both $\mathbf{B_0}$ and the nuclear spin magnetic moment, $\boldsymbol{\mu}$:

$$\sigma_{ij} = \frac{\partial^2 E}{\partial \boldsymbol{\mu}_i \partial \mathbf{B}_{0,j}} \Big|_{\boldsymbol{\mu} = \mathbf{B_0} = 0} \qquad (A9)$$

Using the generalized Hellmann-Feynman (HF) theorem (174), [A9] may be re-expressed as:

$$\sigma_{ij} = \frac{\partial E}{\partial \mathbf{B}_{0j}} \langle \psi_p(\mathbf{r}, \mathbf{B_0}) | \; \partial \mathcal{H}(\boldsymbol{\mu}, \mathbf{B_0})/\partial \boldsymbol{\mu}_{i|\boldsymbol{\mu}=0} |$$
$$\psi_p(\mathbf{r}, \mathbf{B_0}) \rangle_{|\mathbf{B_0}=0} \qquad (A10)$$

where $\mathcal{H}(\boldsymbol{\mu}, \mathbf{B_0})$ is the system Hamiltonian according to KS (see reference 51 for full disclosure), which depends upon both $\mathbf{B_0}$ and $\boldsymbol{\mu}$. The HF theorem allows one to calculate second-order properties (i.e., $\ddot{\sigma}$) using wave functions that are perturbed to first order in one parameter. Detailed evaluations of [A10] exist (51, 175–177): only the most relevant items are summarized below, corresponding to the dominant contributions to paramagnetic shielding.

$\ddot{\sigma}^p$ contributions are expressed similarly when compared with [11]:

$$\sigma_{ij}^p(\text{occ}-\text{occ}) = \sum_{n,m} n_m S_{mn}^{1,i} \langle \psi_n | \frac{i\hat{L}_{Nk}}{r_{Nk}^3} | \psi_m \rangle \quad \text{(A11)}$$

$$\sigma_{ij}^p(\text{occ}-\text{vir}) = 2 \sum_m^{\text{occ}} \sum_r^{\text{vir}} n_m u_{mr}^{1,i} \langle \psi_r | \frac{i\hat{L}_{Nk}}{r_{Nk}^3} | \psi_m \rangle \quad \text{(A12)}$$

where n_m represents the occupation number of the mth MO and $S_{mn}^{1,i}$ and $u_{mr}^{1,i}$ represent overlap coefficients.

REFERENCES

1. Grant DM, Harris RK, eds. 1996. Encyclopedia of Nuclear Magnetic Resonance. New York: Wiley.
2. Butler LG. 2003. An introduction to solution, solid-state and imaging NMR spectroscopy. In: Handbook of Spectroscopy. Gauglitz G, Vo-Dinh T, eds. New York: Wiley.
3. Ramsey NF. 1950. Magnetic shielding of nuclei in molecules. Phys Rev 78:699–703.
4. Ramsey NF. 1951. Dependence of magnetic shielding of nuclei upon molecular orientation. Phys Rev 83:540–541.
5. Ramsey NF. 1952. Chemical effects in nuclear magnetic resonance and in diamagnetic susceptibility. Phys Rev 86:243–246.
6. Pople JA. 1957. The theory of chemical shifts in nuclear magnetic resonance. I. Induced current densities. Proc R Soc (London) A239:541–549.
7. Pople JA. 1962. Theory of chemical shifts. Discuss Faraday Soc 34:7–14.
8. Proctor WG, Yu FC. 1950. The dependence of a nuclear magnetic resonance frequency upon chemical compound. Phys Rev 77:717.
9. Dickinson WC. 1950. Dependence of the fluorine19 nuclear resonance position on chemical compound. Phys Rev 77:736–737.
10. Jameson CJ, De Dios A, Jameson AK. 1990. Absolute shielding scale for phosphorus-31 from gas-phase NMR studies. Chem Phys Lett 167:575–582.
11. Jameson CJ, Jameson AK, Burrell PM. 1980. Fluorine-19 nuclear magnetic shielding scale from gas phase studies. J Chem Phys 73:6013–6020.
12. Laaksonen A, Wasylishen RE. 1995. An absolute chemical shielding scale for tin from NMR relaxation studies and molecular dynamics simulations. J Am Chem Soc 117:392–400.
13. Gee M, Wasylishen RE, Laaksonen A. 1999. A more reliable absolute shielding scale for chlorine: combined experimental and theoretical approach. J Phys Chem A 103:10805–10812.
14. Makulski W, Jackowski K, Antusek A, Jaszunski M. 2006. Gas-phase NMR measurements, absolute shielding scales, and magnetic dipole moments of ^{29}Si and ^{73}Ge nuclei. J Phys Chem A 110:11462–11466.
15. Vaara J, Pyykko P. 2003. Relativistic, nearly basis-set-limit nuclear magnetic shielding constants of the rare gases He-Rn. A way to absolute nuclear magnetic resonance shielding scales. J Chem Phys 118:2973–2976.
16. Jameson CJ, Jameson AK. 1988. Absolute shielding scale for silicon-29. Chem Phys Lett 149:300–305.
17. Jameson CJ, Mason J. 1987. The chemical shift. In: Multinuclear NMR. Mason J, ed. New York: Plenum Press. pp 56–57.
18. Cheeseman JR, Trucks GW, Keith TA, Frisch MJ. 1996. A comparison of models for calculating nuclear magnetic resonance shielding tensors. J Chem Phys 104:5497–5509.
19. Alkorta I, Elguero J. 1998. Ab initio (GIAO) calculations of absolute nuclear shieldings for representative compounds containing $^{1(2)}$H, $^{6(7)}$Li, ^{11}B, ^{13}C, $^{14(15)}$N, ^{17}O, ^{19}F, ^{29}Si, ^{31}P, ^{33}S, and ^{35}Cl nuclei. Struct Chem 9:187–202.
20. Auer AA, Gauss J, Stanton JF. 2003. Quantitative prediction of gas-phase ^{13}C nuclear magnetic shielding constants. J Chem Phys 118:10407–10417.
21. Clawson JS, Anderson KL, Pugmire RJ, Grant DM. 2004. ^{15}N NMR chemical shift tensors of substituted hexaazaisowurtzitanes: the intermediates in the synthesis of CL-20. J Phys Chem A 108:2638–2644.
22. Facelli JC. 2004. Calculations of chemical shieldings. Theory and applications. Concepts Magn Reson A 20:42–69.
23. Ditchfield R. 1974. Self-consistent perturbation theory of diamagnetism. I. A gage-invariant LCAO(linear combination of atomic orbitals) method for NMR chemical shifts. Mol Phys 27: 789–807.
24. Keith TA, Bader RFW. 1993. Calculation of magnetic response properties using a continuous set of gauge transformations. Chem Phys Lett 210:223–231.
25. Kutzelnigg W. 1980. Theory of magnetic susceptibilities and NMR chemical shifts in terms of localized quantities. Israel J Chem 19:193–200.
26. Schindler M, Kutzelnigg W. 1982. Theory of magnetic susceptibilities and NMR chemical shifts in terms of localized quantities. II. Application to some simple molecules. J Chem Phys 76:1919–1933.
27. Lipscomb WN. 1966. The Chemical Shift and Other Second-Order Magnetic and Electric Properties of Small Molecules. In: Advances in Magnetic Resonance. Vol. 2. Waugh JS, ed. New York: Academic Press. pp 138-176.
28. Hansen AE, Bouman TD. 1985. Localized orbital/local origin method for calculation and analysis of NMR shieldings. Applications to carbon-13 shielding tensors. J Chem Phys 82:5035–5047.
29. Fukui H, Baba T, Inomata H. 1996. Calculation of nuclear magnetic shieldings. X. Relativistic effects. J Chem Phys 105:3175–3186.

30. van Lenthe E, Baerends EJ, Snijders JG. 1993. Relativistic regular two-component Hamiltonians. J Chem Phys 99:4597–4610.

31. van Lenthe E, Baerends EJ, Snijders JG. 1994. Relativistic total energy using regular approximations. J Chem Phys 101:9783–9792.

32. Autschbach J, Ziegler, T. 2002. Relativistic computation of NMR shieldings and spin-spin coupling constants. In: Encyclopedia of Nuclear Magnetic Resonance. Vol. 9. Grant DM, Harris RK, eds. Chichester: Wiley. pp 306–323.

33. Kudo K, Fukui H. 2005. Calculation of nuclear magnetic shieldings using an analytically differentiated relativistic shielding formula. J Chem Phys 123: 114102/1–114102/12.

34. Seminario JM, Politzer P, eds. 1995. Modern Density Functional Theory: A Tool for Chemistry. Vol. 2. Amsterdam: Elsevier Science.

35. Gauss J, Stanton JF. 2002. Electron-correlated approaches for the calculation of NMR chemical shifts. In: Advances in Chemical Physics. Vol. 123. Prigogine I, Rice SA, eds. Indianapolis: Wiley. p 355–422.

36. de Dios AC. 1996. Ab initio calculations of the NMR chemical shift. Prog Nucl Magn Reson Spectrosc 29:229–278.

37. Pople JA. 1957. The theory of chemical shifts in nuclear magnetic resonance. II. Interpretation of proton shifts. Proc R Soc (London) A239:550–556.

38. Grutzner JB. 1987. Chemical shift theory. In: Orbital Symmetry and Charge Effects on Chemical Shifts. Lambert JB, Rittner R, eds. Landisville: Norell Press. pp 17–42.

39. Wiberg KB, Hammer JD, Zilm KW, Cheeseman JR, Keith TA. 1998. NMR chemical shifts. I. The role of relative atomic orbital phase in determining the sign of the paramagnetic terms: ClF, CH_3F, CH_3NH_3, FN_3, and HC≡CF. J Phys Chem A 102:8766–8773.

40. Wiberg KB, Hammer JD, Keith TA, Zilm K. 1999. NMR chemical shifts. II. Interpretation of the carbon chemical shifts in monocyclic aromatic compounds and carbenes. J Phys Chem A 103:21–27.

41. Wiberg KB, Hammer JD, Zilm KW, Cheeseman JR. 1999. NMR chemical shifts. III. A comparison of acetylene, allene, and the higher cumulenes. J Org Chem 64:6394–6400.

42. Steiner E, Fowler PW. 2001. Four- and two-electron rules for diatropic and paratropic ring currents in monocyclic Pi systems. Chem Commun 2001:2220–2221.

43. Wiberg KB, Hammer JD, Zilm KW, Keith TA, Cheeseman JR, Duchamp JC. 2004. NMR chemical shifts. Substituted acetylenes. J Org Chem 69:1086–1096.

44. Monaco G, Zanasi R. 2009. On the analysis of some orbital contributions to the current density in circulenes. Int J Quantum Chem 109:243–249.

45. Jameson CJ, Gutowsky HS. 1964. Calculation of chemical shifts. I. General formulation and the Z dependence. J Chem Phys 40:1714–1724.

46. Fowler PW, Steiner E, Havenith RWA, Jenneskens LW. 2004. Current density, chemical shifts and aromaticity. Magn Reson Chem 42 (Special Issue):S68–S78.

47. Feindel KW, Ooms KJ, Wasylishen RE. 2007. A solid-state ^{55}Mn NMR spectroscopy and DFT investigation of manganese pentacarbonyl compounds. Phys Chem Chem Phys 9:1226–1238.

48. Forgeron MAM, Wasylishen RE. 2006. A solid-state ^{95}Mo NMR and computational investigation of dodecahedral and square antiprismatic octacyanomolybdate(IV) anions: is the point-charge approximation an accurate probe of local symmetry? J Am Chem Soc 128:7817–7827.

49. Bieger W, Seifert G, Eschrig H, Grossmann G. 1985. LCAO Xα calculations of nuclear magnetic shielding in molecules. Chem Phys Lett 115:275–280.

50. Friedrich K, Seifert G, Grossmann G. 1990. Nuclear magnetic shielding in molecules. The application of GIAO's in LCAO-Xα-calculations. Z Phys D: At Mol Clusters 17:45–46.

51. Schreckenbach G, Ziegler T. 1995. Calculation of NMR shielding tensors using gauge-including atomic orbitals and modern density functional theory. J Phys Chem 99:606–611.

52. Andrew ER, Bradbury A, Eades RG. 1959. Removal of dipolar broadening of nuclear magnetic resonance spectra of solids by specimen rotation. Nature (London, UK) 183:1802–1803.

53. Lowe IJ. 1959. Free induction decay of rotating solids. Phys Rev Lett 2:285–287.

54. Llor A, Virlet J. 1988. Towards high-resolution NMR of more nuclei in solids: sample spinning with time-dependent spinner axis angle. Chem Phys Lett 152:248–253.

55. Chmelka BF, Mueller KT, Pines A, Stebbins J, Wu Y, Zwanziger JW. 1989. Oxygen-17 NMR in solids by dynamic-angle spinning and double rotation. Nature (London, UK) 339:42–43.

56. Samoson A, Lippmaa E, Pines A. 1988. High-resolution solid-state NMR. Averaging of second-order effects by means of a double-rotor. Mol Phys 65:1013–1018.

57. Farnan I, Grandinetti PJ, Baltisberger JH, Stebbins JF, Werner U, Eastman MA, et al. 1992. Quantification of the disorder in network-modified silicate glasses. Nature (London, UK) 358:31–35.

58. Frydman L, Harwood JS. 1995. Isotropic spectra of half-integer quadrupolar spins from bidimensional magic-angle spinning NMR. J Am Chem Soc 117:5367–5368.

59. Medek A, Harwood JS, Frydman L. 1995. Multiple-quantum magic-angle spinning NMR: a new method for the study of quadrupolar nuclei in solids. J Am Chem Soc 117:12779–12787.

60. Gan Z. 2000. Isotropic NMR spectra of half-integer quadrupolar nuclei using satellite transitions and magic-angle spinning. J Am Chem Soc 122:3242–3243.

61. Bax A, Szeverenyi NM, Maciel GE. 1983. Chemical shift anisotropy in powdered solids studied by 2D FT NMR with flipping of the spinning axis. J Magn Reson (1969-1992) 55:494–497.

62. Bax A, Szeverenyi NM, Maciel GE. 1983. Chemical shift anisotropy in powdered solids studied by two-dimensional cross-polarization magic-angle spinning NMR. J Magn Reson (1969-1992) 51:400–408.

63. Terao T, Fujii T, Onodera T, Saika A. 1984. Switching-angle sample-spinning NMR spectroscopy for obtaining powder-pattern-resolved 2D spectra: measurements of carbon-13 chemical-shift anisotropies in powdered 3,4-dimethoxybenzaldehyde. Chem Phys Lett 107:145–148.

64. Tycko R, Dabbagh G, Mirau PA. 1989. Determination of chemical-shift-anisotropy lineshapes in a two-dimensional magic-angle-spinning NMR experiment. J Magn Reson (1969-1992) 85:265–274.

65. Gan Z. 1992. High-resolution chemical shift and chemical shift anisotropy correlation in solids using slow magic angle spinning. J Am Chem Soc 114:8307–8309.

66. Hu JZ, Wang W, Liu F, Solum MS, Alderman DW, Pugmire RJ, et al. 1995. Magic-angle-turning experiments for measuring chemical-shift-tensor principal values in powdered solids. J Magn Reson Ser A 113:210–222.

67. Gan Z, Grant DM, Ernst RR. 1996. NMR chemical shift anisotropy measurements by RF driven rotary resonance. Chem Phys Lett 254:349–357.

68. Alderman DW, McGeorge G, Hu JZ, Pugmire RJ, Grant DM. 1998. A sensitive, high resolution magic angle turning experiment for measuring chemical shift tensor principal values. Mol Phys 95:1113–1126.

69. Gross JD, Costa PR, Griffin RG. 1998. Tilted n-fold symmetric radio frequency pulse sequences: applications to CSA and heteronuclear dipolar recoupling in homonuclear dipolar coupled spin networks. J Chem Phys 108:7286–7293.

70. de Swiet TM, Tomaselli M, Pines A. 1998. NMR spectra with peaks at the principal values of the chemical shielding tensor. Chem Phys Lett 285:59–63.

71. Ishii Y, Terao T. 1998. Manipulation of nuclear spin Hamiltonians by rf-field modulations and its applications to observation of powder patterns under magic-angle spinning. J Chem Phys 109:1366–1374.

72. Liu SF, Mao JD, Schmidt-Rohr K. 2002. A robust technique for two-dimensional separation of undistorted chemical-shift anisotropy powder patterns in magic-angle-spinning NMR. J Magn Reson 155:15–28.

73. Hester RK, Ackerman JL, Neff BL, Waugh JS. 1976. Separated local field spectra in NMR: determination of structure of solids. Phys Rev Lett 36:1081–1083.

74. Brown SP, Spiess HW. 2001. Advanced solid-state NMR methods for the elucidation of structure and dynamics of molecular, macromolecular, and supramolecular systems. Chem Rev 101:4125–4156.

75. Grinshtein J, Frydman L. 2003. Solid state separated-local-field nmr spectroscopy on half-integer quadrupolar nuclei: principles and applications to borane analysis. J Am Chem Soc 125:7451–7460.

76. Mehring M. 1983. Principles of High Resolution NMR in Solids. New York: Springer-Verlag.

77. Anet FAL, O'Leary DJ. 1991. The shielding tensor. I. Understanding its symmetry properties. Concepts Magn Reson 3:193–214.

78. Hansen AE, Bouman TD. 1989. Calculation, display, and analysis of the nature of nonsymmetric nuclear magnetic resonance shielding tensors: application to three-membered rings. J Chem Phys 91:3552–3560.

79. Wi S, Frydman L. 2002. Quadrupolar-shielding cross-correlations in solid state nuclear magnetic resonance. Detecting antisymmetric components in chemical shift tensors. J Chem Phys 116:1551–1561.

80. Mason J. 1993. Conventions for the reporting of nuclear magnetic shielding (or shift) tensors suggested by participants in the NATO ARW on NMR Shielding Constants at the University of Maryland, College Park, July 1992. Solid State Nucl Magn Reson 2:285–288.

81. Grant DM. 1996. Chemical shift tensors. In: Encyclopedia of Nuclear Magnetic Resonance. Grant DM, Harris RK, eds. New York: Wiley. pp 1298-1321.

82. Jameson CJ. 1998. Reply to 'conventions for tensor quantities used in nuclear magnetic resonance, nuclear quadrupole resonance and electron spin resonance spectroscopy'. Solid State Nucl Magn Reson 11:265–268.

83. Haeberlen U. 1976. High resolution NMR in solids. In: Advances in Magnetic Resonance, Supplement 1. Waugh JS, ed. New York: Academic Press. p 9.

84. Spiess HW. 1978. In: NMR Basic Principles and Progress. Vol. 15. Diehl P, Fluck E, Kosfeld R, eds. Berlin: Springer-Verlag.

85. Zhao X, DeVries JS, McDonald R, Sykes BD. 2007. Determination of the ^{19}F NMR chemical shielding tensor and crystal structure of 5-fluoro-DL-tryptophan. J Magn Reson 187:88–96.

86. Waddell KW, Chekmenev EY, Wittebort RJ. 2005. Single-crystal studies of peptide prolyl and glycyl 15N shielding tensors. J Am Chem Soc 127:9030–9035.

87. Hansen MR, Vosegaard T, Jakobsen HJ, Skibsted J. 2004. ^{11}B Chemical shift anisotropies in borates from ^{11}B MAS, MQMAS, and single-crystal NMR spectroscopy. J Phys Chem A 108:586–594.

88. Gee M, Wasylishen RE, Eichele K, Britten JF. 2000. Phosphorus chemical shift tensors for tetramethyldiphosphine disulfide: A ^{31}P single-crystal NMR, dipolar-chemical shift NMR, and ab initio molecular orbital study. J Phys Chem A 104:4598–4605.

89. Vosegaard T, Byriel IP, Jakobsen HJ. 1997. Characterization of the two rubidium sites in Rb$_2$CrO$_4$ by

[87]Rb single-crystal NMR. J Phys Chem B 101:
8955–8958.

90. Kennedy MA, Ellis PD. 1989. The single-crystal
NMR experiment: an experimentalist's guide. II.
Data analysis and assignment of symmetry-related
tensors. Concepts Magn Reson 1:109–129.

91. Kennedy MA, Ellis PD. 1989. The single-crystal
NMR experiment: an experimentalist's guide. I. Ex-
perimental aspects and symmetry considerations.
Concepts Magn Reson 1:35–47.

92. Kennedy MA, Ellis PD, Jakobsen HJ. 1990.
Cadmium-113 shielding tensors of cadmium com-
pounds. VI. Single-crystal NMR study of the cad-
mium chloride-crown (CdCl2.18-crown-6) complex.
Inorg Chem 29:550–552.

93. Wolff EK, Griffin RG, Waugh JS. 1977. Carbon-13
shielding tensor of a carbon-carbon double bond.
J Chem Phys 67:2387–2388.

94. Buckingham AD, Malm SM. 1971. Asymmetry in
the nuclear magnetic shielding tensor. Mol Phys
22:1127–1130.

95. Kroeker S, Eichele K, Wasylishen RE, Britten JF.
1997. Cesium-133 NMR study of CsCd(SCN)3:
relative orientation of the chemical shielding and
electric field gradient tensors. J Phys Chem B 101:
3727–3733.

96. Vosegaard T, Skibsted J, Jakobsen HJ. 1999. Char-
acterization of $Mo(CO)_6$ by [95]Mo single-crystal
NMR spectroscopy. J Phys Chem A 103:9144–
9149.

97. Eichele K, Wasylishen RE, Corrigan JF, Taylor NJ,
Carty AJ, Feindel KW, Bernard GM. 2002. Phos-
phorus chemical shift tensors of phosphido ligands
in ruthenium carbonyl compounds. ^{31}P NMR spec-
troscopy of single-crystal and powder samples and
ab initio calculations. J Am Chem Soc 124:1541–
1552.

98. Ishii Y, Terao T, Kainosho M. 1996. Relayed ani-
sotropy correlation NMR: determination of dihedral
angles in solids. Chem Phys Lett 256:133–140.

99. Yao X, Hong M. 2002. Determination of Ca
chemical shift tensor orientation in peptides by
dipolar-modulated chemical shift recoupling NMR
spectroscopy. J Am Chem Soc 124:2730–2738.

100. VanderHart DL, Gutowsky HS, Farrar TC. 1969.
N.M.R. study of barium phosphorofluoridate:
phosphorus-31 and fluorine-19 chemical-shift ani-
sotropies and the absolute sign of the fluorine-
phosphorus coupling constant. J Chem Phys
50:1058–1065.

101. VanderHart DL, Gutowsky HS. 1968. Rigid-lattice
N.M.R. moments and line shapes with chemical-
shift anisotropy. J Chem Phys 49:261–271.

102. Zilm KW, Grant DM. 1981. Carbon-13 dipolar
spectroscopy of small organic molecules in argon
matrixes. J Am Chem Soc 103:2913–2922.

103. Zilm KW, Beeler AJ, Grant DM, Michl J, Chou
TC, Allred EL. 1981. Carbon-13 magnetic reso-
nance dipolar spectroscopy. Orientation of the

chemical shift tensor in cyclopropane. J Am Chem
Soc 103:2119–2120.

104. Eichele K, Wasylishen RE. 1994. The dipolar-split-
ting-ratio method—a convenient approach to the
analysis of dipolar-chemical-shift NMR spectra of
static powder samples. J Magn Reson Ser A
106:46–56.

105. Saika A, Slichter CP. 1954. A note on the fluorine
resonance shifts. J Chem Phys 22:26–28.

106. Slichter CP. 1963. Principles of Magnetic Reso-
nance. Seitz F, ed. New York: Harper & Row.

107. Karplus M, Das TP. 1961. Theory of localized con-
tributions to chemical shift. Applications to fluoro-
benzenes. J Chem Phys 34:1683–1692.

108. te Velde G, Bickelhaupt FM, Baerends EJ, Fonseca
Guerra C, Van Gisbergen SJA, Snijders JG, et al.
2001. Chemistry with ADF. J Comput Chem 2:931–
967.

109. Kohn W, Sham LJ. 1965. Self-consistent equations
including exchange and correlation effects. Phys
Rev 140:A1133–A1138.

110. Karplus M, Pople JA. 1963. Carbon N.M.R. [nu-
clear magnetic resonance] chemical shifts in conju-
gated molecules. J Chem Phys 38:2803–2807.

111. Rozhenko AB, Schoeller WW, Povolotskii MI.
1999. Ab initio calculation of NMR shielding in
phosphaalkenes X-P=CY2. Magn Reson Chem
7:551–563.

112. Zilm KW, Conlin RT, Grant DM, Michl J. 1980.
Low-temperature carbon-13 magnetic resonance of
solids. I. Alkenes and cycloalkenes. J Am Chem
Soc 102:6672–6676.

113. Chesnut DB, Quin LD. 1994. Characterization of
NMR deshielding in phosphole and the phospholide
ion. J Am Chem Soc 16:9638–9643.

114. Barrie PJ, Groombridge CJ, Mason J, Moore EA.
1994. Nitrogen-15 nuclear magnetic shielding tensors
in nitrite and nitrate ion. Experimental and theoretical
determinations. Chem Phys Lett 19:491–496.

115. Wiberg KB, Hammer JD, Keith TA, Zilm K. 1997.
^{13}C NMR chemical shifts of methyl cation and
anion: a relationship between chemical shift and
charge? Tetrahedron Lett 8:323–326.

116. Chesnut DB. 1997. Ab initio NMR chemical shield-
ings in the neutral and charged 7-phosphabi-
cyclo[2.2.1]heptane, -heptene, and -heptadiene
systems: the largest predicted downfield shift for a
conventional organophosphorus molecule. Chem
Phys 24:133–141.

117. Kaupp M, Malkina OL. 1998. Density functional
analysis of ^{13}C and ^{1}H chemical shifts and bonding
in mercurimethanes and organomercury hydrides:
the role of scalar relativistic, spin-orbit, and substit-
uent effects. J Chem Phys 108:3648–3659.

118. Gilbert TM, Ziegler T. 1999. Prediction of 195Pt
NMR chemical shifts by density functional theory
computations: the importance of magnetic coupling
and relativistic effects in explaining trends. J Phys
Chem A 103:7535–7543.

119. Autschbach J. 2008. Analyzing NMR shielding tensors calculated with two-component relativistic methods using spin-free localized molecular orbitals. J Chem Phys 28:164112/1–164112/11.

120. Arduengo AJ, Dixon DA, Kumashiro KK, Lee C, Power WP, Zilm KW. 1994. Chemical shielding tenser of a carbene. J Am Chem Soc 16:6361–6367.

121. Schurko RW, Hung I, Macdonald CLB, Cowley AH. 2002. Anisotropic NMR interaction tensors in the decamethylaluminocenium cation. J Am Chem Soc 24:13204–13214.

122. Schreckenbach G, Ziegler T. 1996. The calculation of NMR shielding tensors based on density functional theory and the frozen core approximation. Int J Quantum Chem 60:753–766.

123. Schreckenbach G, Ziegler T. 1997. Calculation of NMR shielding tensors based on density functional theory and a scalar relativistic Pauli-type Hamiltonian. The application to transition metal complexes. Int J Quantum Chem 61:899–918.

124. Wolff SK, Ziegler T. 1998. Calculation of DFT-GIAO NMR shifts with the inclusion of spin-orbit coupling. J Chem Phys 109:895–905.

125. Wolff SK, Ziegler T, van Lenthe E, Baerends EJ. 1999. A GIAO-ZORA implementation. J Chem Phys 110:7689–7698.

126. Atkins P. 1998. Physical Chemistry. New York: W. H. Freeman and Company.

127. Guerra CF, Snijders JG, Te Velde G, Baerends EJ. 1998. Towards an order-N DFT method. Theor Chem Acc 99:391–403.

128. Baerends EJ, Autschbach J, Bérces A, Bo C, Boerrigter PM, Cavallo L, et al. ADF. 2005.01. Amsterdam: SCM, Theoretical Chemistry, Vrije Universiteit; 2005.

129. Schreckenbach G, Ziegler T. 1997. Calculation of the G-tensor of electron paramagnetic resonance spectroscopy using gauge-including atomic orbitals and density functional theory. J Phys Chem A 101:3388–3399.

130. Becke AD. 1988. Density-functional exchange-energy approximation with correct asymptotic-behavior. Phys Rev A 38:3098–3100.

131. Lee C, Yang W, Parr RG. 1988. Development of the Colle-Salvetti correlation-energy formula into a functional of the electron density. Phys Rev B 37:785–789.

132. Jackowski K, Raynes WT. 1977. Density-dependent magnetic shielding in gas phase carbon-13 NMR. Mol Phys 34:465–475.

133. Jameson AK, Jameson CJ. 1987. Gas-phase carbon-13 chemical shifts in the zero-pressure limit: refinements to the absolute shielding scale for carbon-13. Chem Phys Lett 134:461–466.

134. Böhm MC, Schulte J, Ramírez R. 2000. Nuclear quantum effects in calculated NMR shieldings of ethylene; a Feynman path integral—ab initio study. Chem Phys Lett 332:117–124.

135. Ruud K, Åstrand PO, Taylor PR. 2001. Zero-point vibrational effects on proton shieldings: functional-group contributions from ab initio calculations. J Am Chem Soc 123:4826–4833.

136. Chesnut DB. 2003. Scaled DFT chemical shieldings. Chem Phys Lett 380:251–257.

137. Orendt AM, Facelli JC, Beeler AJ, Reuter K, Horton WJ, Cutts P, et al. 1988. Low-temperature carbon-13 magnetic resonance. VIII. Chemical shielding anisotropy of olefinic carbons. J Am Chem Soc 110:3386–3392.

138. SCM. ADF-GUI 2008.01. Amsterdam, The Netherlands. Available at: www.scm.com.2008.

139. Hindermann DK, Cornwell CD. 1968. Vibrational corrections to the nuclear-magnetic shielding and spin-rotation constants for hydrogen fluoride. Shielding scale for fluorine-19. J Chem Phys 48:4148–4154.

140. Gauss J, Stanton JF. 1996. Perturbative treatment of triple excitations in coupled-cluster calculations of nuclear magnetic shielding constants. J Chem Phys 104:2574–2583.

141. Manninen P, Ruud K, Lantto P, Vaara J. 2005. Leading-order relativistic effects on nuclear magnetic resonance shielding tensors. J Chem Phys 122:114107/1–114107/8.

142. Manninen P, Ruud K, Lantto P, Vaara J. 2006. Leading-order relativistic effects on nuclear magnetic resonance shielding tensors [Erratum to document cited in CA143:018527]. J Chem Phys 124:149901/1–149901/2.

143. Chan JCC, Eckert H. 2001. Density functional study of ^{19}F chemical shielding tensors: a systematic investigation with respect to basis sets and hybrid functionals. Theochem 535:1–8.

144. De Leeuw FH, Dymanus A. 1973. Magnetic properties and molecular quadrupole moment of hydrogen fluoride and hydrogen chloride by molecular-beam electric-resonance spectroscopy. J Mol Spectrosc 48:427–445.

145. Ditchfield R. 1981. Theoretical studies of the temperature dependence of magnetic shielding tensors: molecular hydrogen, hydrogen fluoride, and lithium hydride. Chem Phys 63:185–202.

146. Montana AJ, Zumbulyadis N, Dailey BP. 1976. Fluorine-19 and phosphorus-31 magnetic shielding anisotropies and the fluorine-phosphorus-fluorine bond angle of thiophosphoryl fluoride in a smectic liquid crystal solvent. J Chem Phys 65:4756–4760.

147. Zumbulyadis N, Dailey BP. 1973. Fluorine-19 and phosphorus-31 magnetic resonance spectra of phosphorus trifluoride in nematic solution. Mol Phys 26:777–782.

148. Jaszunski M. 2004. Ab initio study of the shielding and spin-spin coupling constants in ClF_3, PF_3 and PF_5. Chem Phys Lett 385:122–126.

149. Duncan TM. 1990. A Compilation of Chemical Shift Anisotropies. Chicago: The Farragut Press.

150. Tossell JA, Lazzeretti P. 1987. Coupled Hartree-Fock calculations of phosphorus-31 NMR shieldings

in phosphorous fluorides and phosphate(3-). J Chem Phys 86:4066–4069.

151. Brosnan SGP, Edmonds DT. 1980. Proton fine structure in the nuclear quadrupole double resonance spectrum of ^{17}O naturally abundant in ice at 77K. J Mol Struct 58:23–32.

152. Spiess HW, Garrett BB, Sheline RK, Rabideau SW. 1969. Oxygen-17 quadrupole coupling parameters for water in its various phases. J Chem Phys 51:1201–1205.

153. Jameson CJ. 1989. Theoretical and physical aspects of nuclear shielding. Nucl Magn Reson 18:1–33.

154. Bruna PJ, Hachey MRJ, Grein F. 1997. Benchmark ab initio calculations of formaldehyde, H2CO. Theochem 400:177–221.

155. Wasylishen RE, Mooibroek S, Macdonald JB. 1984. A more reliable oxygen-17 absolute chemical shielding scale. J Chem Phys 81:1057–1059.

156. Wasylishen RE, Bryce DL. 2002. A revised experimental absolute magnetic shielding scale for oxygen. J Chem Phys 117:10061–10066.

157. Vaara J, Lounila J, Ruud K, Helgaker T. 1998. Rovibrational effects, temperature dependence, and isotope effects on the nuclear shielding tensors of water: a new ^{17}O absolute shielding scale. J Chem Phys 109:8388–8397.

158. Duer MJ. 2004. Introduction to Solid-State NMR Spectroscopy. Cornwall: Blackwell Publishing.

159. Sterzel M, Autschbach J. 2006. Toward an accurate determination of ^{195}Pt chemical shifts by density functional computations: the importance of unspecific solvent effects and the dependence of Pt magnetic shielding constants on structural parameters. Inorg Chem 45:3316–3324.

160. ADF2005.01. Amsterdam: SCM, Theoretical Chemistry, Vrije Universiteit.

161. Wolinski K, Hinton JF, Pulay P. 1990. Efficient implementation of the gauge-independent atomic orbital method for NMR chemical-shift calculations. J Am Chem Soc 112:8251–8260.

162. Parr RG, Yang W. 1989. Density-Functional Theory of Atoms and Molecules. New York: Oxford University Press.

163. Wilk L, Vosko SH. 1977. Investigation of the spin-density functional method for calculating spin-magnetic-moment densities. Phys Rev A: At Mol Opt Phys 15:1839–1846.

164. Vosko SH, Wilk L, Nusair M. 1980. Accurate spin-dependent electron liquid correlation energies for local spin density calculations: a critical analysis. Canadian J Phys 58:1200–1211.

165. Perdew JP. 1986. Density-functional approximation for the correlation-energy of the inhomogeneous electron-gas. Phys Rev B 33:8822–8824.

166. Perdew JP. 1986. Correction. Phys Rev B 34:7406–7406.

167. Vignale G, Rasolt M. 1987. Density-functional theory in strong magnetic fields. Phys Rev Lett 59:2360–2363.

168. Vignale G, Rasolt M. 1989. Density-functional theory in strong magnetic fields [Erratum to document cited in CA108:27096w]. Phys Rev Lett 62:115.

169. Lee C, Parr RG. 1990. Exchange-correlation functional for atoms and molecules. Phys Rev A: At Mol Opt Phys 42:193–200.

170. Perdew JP, Burke K, Ernzerhof M. 1996. Generalized gradient approximation made simple. Phys Rev Lett 77:3865–3868.

171. Zhang YK, Yang WT. 1998. Comment on "Generalized gradient approximation made simple". Phys Rev Lett 80:890.

172. Zhang Y, Wu A, Xu X, Yan Y. 2006. OPBE: a promising density functional for the calculation of nuclear shielding constants. Chem Phys Lett 421:383–388.

173. Pople JA, Krishnan R, Schlegel HB, Binkley JS. 1979. Derivative studies in Hartree-Fock and Moller-Plesset theories. Int J Quantum Chem: Quantum Chem Sympos 13:225–241.

174. Levine IN. 2000. The Hellman–Feynman theorem. In: Quantum Chemistry. Upper Saddle River: Prentice-Hall. pp 469–472.

175. Schreckenbach G. Relativity and Magnetic Properties. A Density Functional Study. Calgary: University of Calgary. 1996.

176. Schreckenbach G, Ziegler T. 1998. Density functional calculations of NMR chemical shifts and ESR g-tensors. Theor Chem Acc 99:71–82.

177. Bouten R, Baerends EJ, van Lenthe E, Visscher L, Schreckenbach G, Ziegler T. 2000. Relativistic effects for NMR shielding constants in transition metal oxides using the zeroth-order regular approximation. J Phys Chem A 104:5600–5611.

BIOGRAPHIES

Cory M. Widdifield received B.Sc and M.Sc degrees in chemistry from the University of Windsor under the supervision of Prof. Robert W. Schurko. In 2008, he enrolled in the chemistry Ph.D program at the University of Ottawa, under the supervision of Prof. David L. Bryce. His current research focuses on developing $^{79/81}$Br and ^{127}I solid-state NMR of ionic bromide and iodide systems.

Robert W. Schurko was born in Winnipeg, Manitoba. He completed his B.Sc. (Honours) and M.Sc. at the University of Manitoba with Ted Schaefer, and Ph.D. at Dalhousie University with Rod Wasylishen. He is currently an Associate Professor at the University of Windsor in Windsor, Ontario, Canada, where he has been since 2000. Rob's research interests focus around the application and development of solid-state NMR techniques, X-ray crystallography and first principles calculations for the characterization of materials at the molecular level, including organometallics, main group and transition metal complexes, nanoparticles, pharmaceuticals, and porous/layered solids.